

# Inverse Design of Metal-Organic Frameworks Using Quantum Natural Language Processing

*Shinyoung Kang, Jihan Kim\**

Department of Chemical and Biomolecular Engineering, Korea Advanced Institute of  
Science and Technology (KAIST) 291 Daehak-ro, Yuseong-gu, Daejeon 34141, Republic of  
Korea

\*E-mail: [jihankim@kaist.ac.kr](mailto:jihankim@kaist.ac.kr), Phone: +82-42-350-7311 (Corresponding author)

## ABSTRACT

In this study, we explore the potential of using quantum natural language processing (QNLP) to inverse design metal-organic frameworks (MOFs) with targeted properties. Specifically, by analyzing 150 hypothetical MOF structures consisting of 10 metal nodes and 15 organic ligands, we categorize these structures into four distinct classes for pore volume and H<sub>2</sub> uptake values. We then compare various QNLP models (i.e. the bag-of-words, DisCoCat (Distributional Compositional Categorical), and sequence-based models) to identify the most effective approach to process the MOF dataset. Using a classical simulator provided by the IBM Qiskit, the bag-of-words model is identified to be the optimum model, achieving validation accuracies of 85.7% and 86.7% for binary classification tasks on pore volume and H<sub>2</sub> uptake, respectively. Further, we developed multi-class classification models tailored to the probabilistic nature of quantum circuits, with average test accuracies of 88.4% and 80.7% across different classes for pore volume and H<sub>2</sub> uptake datasets. Finally, the performance of generating MOF with target properties showed accuracies of 93.5% for pore volume and 89% for H<sub>2</sub> uptake, respectively. Although our investigation covers only a fraction of the vast MOF search space, it marks a promising first step towards using quantum computing for materials design, offering a new perspective through which to explore the complex landscape of MOFs.

## Introduction

As the idea of quantum computers first arose in 1982 following Feynman's proposal<sup>1</sup>, many theoretical and experimental works have explored the possibilities to accelerate scientific discovery using this technology. Recently, quantum machine-learning (QML) algorithms have surfaced as a promising alternative to their classical machine-learning approaches<sup>2</sup> to develop materials based on the advantages of quantum computers<sup>3</sup>. This shift is attributed to the algorithmic speed-up of quantum computers based on quantum parallelism and the non-classical correlations arising from quantum entanglement<sup>3</sup>. At the core of QML lies the exploitation of quantum bits (qubits), which unlike classical bits, can exist in a superposition of states and be entangled with one another. This allows quantum algorithms to perform complex calculations more efficiently, leveraging quantum parallelism to explore multiple possibilities simultaneously<sup>4</sup>. Current quantum computing technology is categorized as being at the Noisy Intermediate-Scale Quantum (NISQ) stage, which refers to intermediate number of qubits (approximately 100 qubits), while lacking the capacity for large-scale error correction<sup>3</sup>. Consequently, the NISQ era poses significant challenges as it features quantum computers with a limited number of qubits that are prone to errors<sup>5</sup>.

These limitations have led to the development of QML algorithms for NISQ devices based on shallow-circuit depth and a hybrid quantum-classical approach, which delegates a part of the computation to a classical processor<sup>3, 6</sup>. To this end, many researchers have suggested methods to apply QML in solving complex problems in materials science and chemistry by focusing on compatible QML methodologies. Specifically, Kanno et al. demonstrated that the physicochemical properties of the periodic materials can be successfully calculated with this concept by adopting a restricted Boltzmann machine-based variational quantum eigensolver (RBM-based VQE) for the band structure calculation of graphene<sup>7</sup>. This approach was further developed by Sajjan et al. as conduction bands of monolayer transition metal dichalcogenides, MoS<sub>2</sub> and WS<sub>2</sub>, were simulated and filtered based on angular momentum symmetry<sup>2</sup>. Scientific endeavors to further extend the search space of materials with quantum computing led to the development of a QML algorithm for property prediction. Brown et al. introduced a quantum variational eigensolver-based circuit learning method to estimate the phases of high-entropy alloys (HEAs), with the model's performance nearing that of classical artificial neural network (ANN) models in classifying ternary and binary phases<sup>8</sup>. Naseri et al. explored the use of a supervised hybrid quantum-classical ML algorithm for the binary classification of ABO<sub>3</sub> perovskite structures, showcasing the applicability of QML in materials discovery<sup>9</sup>. Despite these advancements, previous studies have largely focused on

relatively simple periodic systems such as TMDs and perovskite structures, with challenges arising in scaling to larger systems like metal-organic frameworks (MOFs) due to the difficulty of individually encoding atoms into a constrained qubit resource.

To address this limitation, we adopted using quantum natural language processing (QNLP) as a novel approach to efficiently represent materials. QNLP is an emerging field that combines quantum computing with natural language processing (NLP), aimed to utilize the principles of quantum mechanics to process and analyze natural language data more efficiently than classical computing methods. This concept was first introduced by Coecke et al.<sup>10, 11</sup> based on the idea that quantum computing is naturally suited to process high-dimensional tensor products and that NLP can utilize vector spaces to describe sentences<sup>12</sup>. In quantum computing, the state of a quantum system with multiple qubits is represented by a vector in a high-dimensional Hilbert space<sup>13</sup>. Since the operations or transformations applied to these qubits are represented by matrices, any quantum operations to the system of qubits are processed by performing tensor products of matrices to calculate the new state of the system<sup>4</sup>. This enables the representation of the complex, high-dimensional states and transformations fundamental to quantum computing. In the context of NLP, sentences can be represented in high-dimensional vector spaces, and the relationships between words involve complex transformations within these spaces. The potential of QNLP arises from its natural and efficient use of such calculations due to its inherent ability to operate in high-dimensional Hilbert spaces. As such, a hybrid quantum-classical algorithm based on QNLP was adopted from the previous studies for sentence generation<sup>14</sup> and music composition<sup>15</sup>. For sentence generation, Karamlou et al. performed a comparative study on two types of datasets: binary classification for identifying different sentence topics and multi-class classification for identifying news headlines. QNLP models were separately trained for these datasets, and these quantum models provided feedback to the classical model for sentence generation, resulting in 22 and 11 correct sentence generations out of 30 attempts for binary and multi-class classification models, respectively, in the classical simulator provided by the IBM Qiskit<sup>14</sup>. A similar quantum-classical framework was applied to music generation by Miranda et al<sup>15</sup>. The QNLP model was developed to identify types of music (between rhythmic and melodic), resulting in a test accuracy of 76% on real quantum hardware<sup>15</sup>. However, to the best of our knowledge, QNLP has yet to be applied to any molecular structures or materials.

In this work for the first time, we explored the possibility of using QNLP to model metal-organic frameworks (MOFs), which are crystalline porous materials consisting of metal clusters and organic ligands<sup>16</sup>.

The choice of MOF as our target material was based on its modular nature, which is akin to how words form sentences. Their structural and functional characteristics can be designed through the rational selection of topologies and constituent building blocks, including organic ligands and metal-containing units<sup>17-19</sup>. This characteristic resembles how sentences with various subjects are formed based on the choice of words. This versatile architecture allows MOFs to be widely used in many applications such as gas sensors<sup>20</sup>, drug delivery<sup>21</sup>, gas storage<sup>22</sup>, and separation<sup>23</sup>. However, the challenge in rationalizing component choices arises from the extensive search space required to select combinations of building blocks and topology. As the search space for MOFs continues to expand, addressing the curse of dimensionality becomes critical. This concern was previously emphasized by Brown et al. in the context of designing periodic materials with large degrees of freedom such as HEAs<sup>8</sup>.

We adopted the hybrid quantum-classical method to construct a MOF generation framework with user-desired properties. Pore volume and H<sub>2</sub> uptake were chosen as target properties of interest as they reflect the physical and chemical properties of MOF structures, respectively. The former reflects a direct result of the MOF's structural characteristics, whereas the latter stems from the MOFs' ability to adsorb and interact with guest molecules, an attribute linked to the interplay of their geometrical<sup>24, 25</sup>, and chemical properties<sup>26</sup>, which amplifies the challenge of the task. By representing MOFs in terms of their constituent building blocks and topology, we simplified their qubit representation, thereby making quantum resources more accessible for the study of complex materials. The overall workflow of this work is summarized in Figure 1. Initially, we describe the construction of MOF datasets, featuring a simplified representation of 150 MOF structures. These are categorized by target property classes, such as low, moderately low, moderately high, and high pore volume or H<sub>2</sub> uptake classes (Figure 1a). Next, we rationalized our choice of the QNLP models based on the comparative study among four different approaches: the bag-of-words, DisCoCat (Distributional Compositional Categorical), and two sequence-based models (Figure 1b). The multi-classification models were then developed, exploring ways to overcome the statistical limitations inherent to the QNLP model selected from the comparative study (Figure 1c). These limitations stem from the probabilistic nature of the chosen QNLP model. As a result, QNLP models for categorizing target classes were developed with average test accuracies of 88.4% and 80.7% for pore volume and H<sub>2</sub> uptake datasets, respectively. Finally, these models were integrated with the classical MOF generation process, which generates text-based MOF input by randomly selecting topology and building blocks in each component's search space (Figure 1d). The QNLP models functioned as answer sheets, providing

feedback to the classical generation loop to navigate the search space of MOF building blocks correctly. To test the performance of the overall process for generating MOF with target property, the model was tested on a classical Aer simulator by the IBM Qiskit<sup>27</sup> to generate MOFs with low, moderately low, moderately high, and high pore volumes and H<sub>2</sub> uptakes. The average generation accuracies for MOFs with desired pore volume and H<sub>2</sub> uptake were 93.5% and 89%, respectively. In the last section, we discussed the extensibility of QNLP to other complex periodic materials based on ‘sequence’ as one of the promising parameters for representing chemical structures. Our study not only circumvents the qubit limitation but also opens new avenues for applying quantum machine learning in the exploration and design of advanced materials.

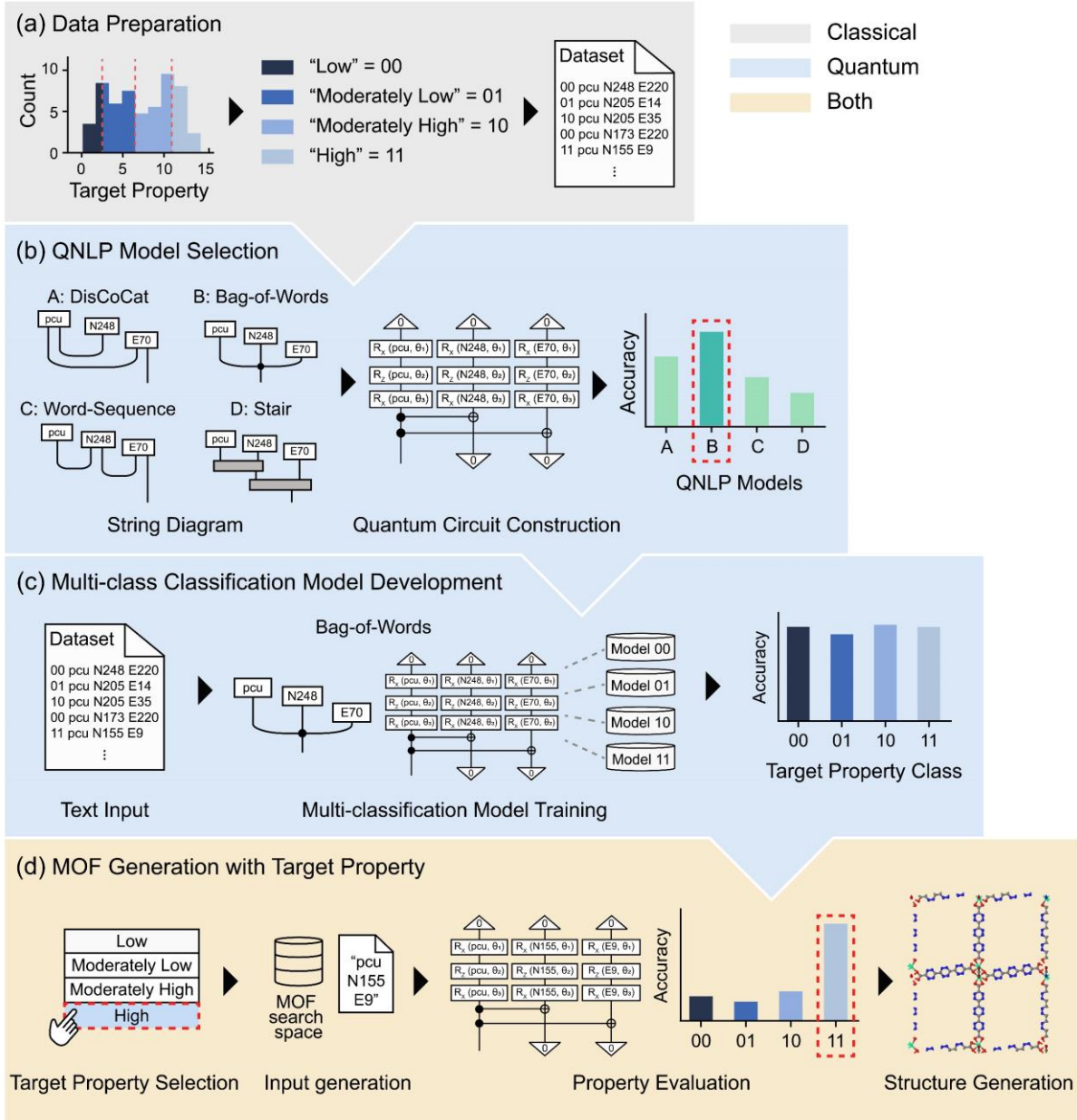


**Figure 1.** General overview of the study. Gray, blue, and yellow boxes indicate the classical computer-based, quantum computer-based, and hybrid quantum-classical computer-based processes, respectively. **(a)** MOF dataset construction from target property distributions encoded into four classes, and it is transformed into the text dataset consisting of the target class and its corresponding MOF name. **(b)** Comparative study among QNLP model candidates. Models A, B, C, and D refer to DisCoCat, bag-of-words (BoW), word-sequence, and stair models, respectively. **(c)** Multi-classification model development based on the choice of QNLP model from the QNLP model selection step. Four binary classification models by target property type (pore volume and H<sub>2</sub> uptake) are combined to complete a multi-classification framework. **(d)** MOF generation framework to build MOF structure with the desired target property.

## Results and Discussion

### Building the MOF Dataset

The MOF dataset in this work consists of a single pcu topology, 10 types of metal clusters (labeled as nodes in this work), and 15 types of organic ligands (labeled as edges in this work), with the number being small considering the current limitations in quantum resource availability (Figure S1). Chemical molecules and materials possess complex degrees of freedom that influence their mechanical and chemical properties. This complexity arises because the individual components of chemical compounds are directly linked to their properties. For instance, MOFs that share the same types of metal nodes and ligand edges but differ in their topology (i.e., polymorphism) result in significant differences in surface area, which applies to the case of MIL-101<sup>28</sup>, MIL-88<sup>29</sup>, and MIL-53<sup>30</sup>. Furthermore, MOFs with identical topology and metal nodes but different organic ligands exhibit variations in chemical and mechanical properties, such as gas uptake and pore diameter<sup>31</sup>. This suggests that introducing a single type of building block adds more than just a single degree of freedom, thereby complicating the selection of building blocks given the manageable dataset size for the NISQ devices. Consequently, the dataset was restricted to include only one topology. This decision was based on the direct relationship between topology and our target properties, aiming to minimize the impact of variations in the building blocks, metal nodes, and organic ligands.

A pcu topology, one of the most fundamental topologies, was selected for its straightforward pore structure and high symmetry owing to a cubic arrangement<sup>32</sup>. The MOF building blocks were chosen based on structural similarity in the molecular framework to ensure a broad and consistent distribution of target properties of pore volume and H<sub>2</sub> uptake. For the metal clusters, we considered structural analogs that form rod-like connections with the ligands. These clusters are composed of two metals covered by oxygen functional groups, represented by the formula, M<sub>2</sub>C<sub>6</sub>O<sub>12</sub>X<sub>6</sub> (where M denotes the metal and X represents the connection point with the ligand, as shown in Figure S1a). For the organic ligands, cyclic compounds with various lengths ranging from 3.56 to 16.12 Å were considered (Figure S1b). The datasets were evenly divided into four classes with regard to the aforementioned target properties: (1) low, (2) moderately low, (3) moderately high, and (4) high, as shown in Figures 2a and c. The decision to use multiple target property classes rather than a simple binary classification (e.g. low and high) was made to enable the generation of MOFs within the more refined user-desired target property class. The class boundary was determined to ensure an even distribution among the

classes, with 38 samples each for the low and high classes and 37 samples each for the moderately low and moderately high classes in terms of pore volume and H<sub>2</sub> uptake, thereby maintaining the uniformity of the dataset. Finally, low, moderately low, moderately high, and high classes were encoded into classical labels of 00, 01, 10, and 11, respectively, to directly compare with quantum models' prediction, as depicted in Figure 1a. The next section will provide a detailed explanation of how the outcomes of the quantum model are processed and compared with the true labels. The MOF datasets for QNLP model training were then prepared with the target property class and its corresponding MOF name listed by topology, node, and edge names. For example, the MOF named 'pcu N248 E220' with low pore volume, was mapped into the label '00 pcu N248 E220' in our MOF dataset.

Figures 2b and d show the influence of the building blocks on the classes of pore volumes and H<sub>2</sub> uptakes by showing the number of occurrences per building block in each class. The counts can be considered as the numerical contribution of the individual building blocks for each class. Considering that 15 and 10 MOF structures can be created per node and edge type, the individual building blocks that appeared more than 50% of possible structures in a class were considered 'class-significant' building blocks. This indicates that the MOFs with the corresponding building block are highly likely to possess that class property. Therefore, the 6-count is considered the boundary for class-significance for node and edge type. Based on this assumption, the impact of the organic ligands was higher than that of the metal clusters on both datasets, showing the class-significance in every class with many polarized counts. The distribution of the class-significant building blocks in each class was also similar in order of 00, 11, 10, and 01. Understanding the distribution of class-significant building blocks is crucial, as it directly affects the difficulty of model training. For instance, generating MOFs with the 00-class property (low pore volume or low H<sub>2</sub> uptake) is considerably easier than generating MOFs with the 01-class property (moderately low pore volume or moderately low H<sub>2</sub> uptake) owing to the higher frequency of occurrences focused on specific building blocks, such as E70 and E220, in both datasets. Consequentially, there is a variation in the level of difficulty across the classes despite the even distribution of sample numbers, reflecting the continuous nature of MOF properties. The similarity in class distribution between the pore volume and H<sub>2</sub> uptake datasets can be attributed to their linear correlation, as illustrated in Figure S2.

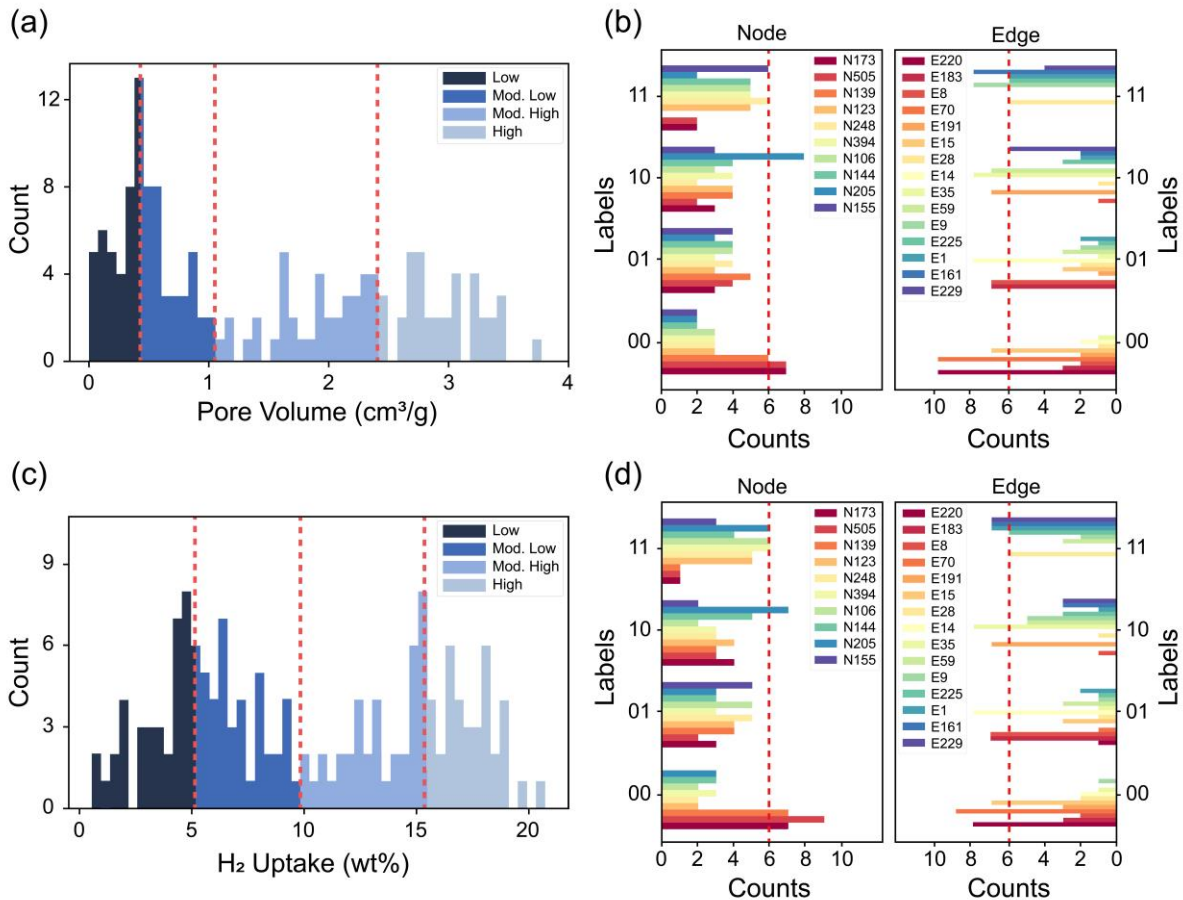


**Figure 2.** Distributions of 150 hypothetical MOFs based on (a) pore volumes and (c) H<sub>2</sub> uptakes. The datasets were divided into four classes based on 25, 50, and 75 percentiles of the pore volume and H<sub>2</sub> uptake values. Vertical dotted lines indicate corresponding class boundaries. Counts of classes per node (metal cluster) type and edge (organic ligands) type based on (b) pore volumes and (d) H<sub>2</sub> uptakes. Labels 00, 01, 10, and 11 represent low, moderately low, moderately high, and high pore volumes and H<sub>2</sub> uptake, respectively. Vertical red dotted lines represent a count boundary of the class-significance.

## Mapping the MOF Dataset onto Different QNLP Models

For quantum model training, the aforementioned MOF dataset needs to be transformed into quantum circuits, which requires pre-processing of the dataset based on the choice of QNLP models. In order to implement a quantum model for the property classification, four QNLP models were explored: BoW model, DisCoCat model, and the two word-sequence models. The MOF representation of topology, node, and edge was mapped into a high-dimensional vector space where each dimension corresponds to a unique component of the

MOF. The method by which these components are processed, akin to grammatical structure, can be mathematically depicted through tensor products, with these operations on the component vectors that vary distinctively across different QNLP model types. The graphical representations of these complex vector spaces and the mathematical functions connecting them are known as string diagrams<sup>33</sup> as illustrated in Figure 1b and Figure 3a. Based on these diagrams and the choice of ansatz, the quantum circuits can be constructed as MOF component vectors are mapped into individual qubits, and quantum gate operations implement the tensor products. The ansatz is a proposed structure of quantum circuit consisting of adjustable circuit parameters such as the number of qubits or unitary operations within a given vector space. The qubits are initially in the  $|0\rangle$  states and then evolve through a sequence of unitary operations (i.e. gates). Based on the choice of the IQP (Instantaneous Quantum Polynomial) ansatz, the unitary operations employed were Hadamard gate (H) and rotation gates of  $R_x(\theta)$  and  $R_z(\theta)$ , which rotate a qubits state around the respective axis by an angle,  $\theta$ . Readers might refer to the method section for further explanation about the choice of ansatz.

In this paper, we will focus on the BoW model to specifically explain how the QNLP model transforms classical data into a quantum circuit and identify which components of the quantum circuits are optimized against the true labels. For information on other QNLP models, readers may refer to Note S1. The BoW model, based on a Frobenius algebra, transforms text into a sparse vector of word counts and represents the output as the component-wise multiplication of these vectors,  $s$ <sup>33</sup>. That is, each MOF component vector (topology, node, and edge) is mapped to the high-dimensional vector space obtained from the component-wise multiplication, independent of word order. In the associated string diagram, each component vector is represented as a separate box and the component-wise multiplication is represented as a ‘merge-dot’ as shown in Figure 3a. The focus of this model would be on the presence or absence of specific component vectors over the explicit connections among them to indicate grammatical structure or sequence in other models such as DisCoCat and the word-sequence models (Note S1). The transformation into a quantum circuit involves mapping individual MOF component vectors onto separate qubits, with unitary operations then used to manipulate the overall quantum state of these qubits (Figure 3b). The number of qubits per component vector varies depending on the task, and this will be discussed in the next section. Initially, all qubits representing corresponding MOF components are in a default state,  $|0\rangle$  (Figure 3b(i)). The quantum state of each qubit is then uniquely altered through a sequence of unitary operations (Figure 3b(ii)), and the rotational angles of these operations,  $\theta_{c,n}$  (where  $c$  and  $n$  represent MOF component and integer, respectively), are quantum circuit

parameters optimized through quantum machine learning. The merge-dot of the string diagram is encoded as the controlled-not gates (Figure 3b(iii)). Finally, the predicted class label is determined by measuring the quantum circuit. Since the controlled-not gates represent the component-wise multiplication characteristic of the BoW model, a control qubit delivers the predicted class label. This qubit, associated with the predicted class label and delivering the outcome of the circuit measurement, is referred to as an ‘open’ wire qubit, as it is represented by the wire coming out of the component in the quantum circuit<sup>33</sup> (Figures 3b). For instance, in a binary classification task for pore volume as an example, ‘low’ and ‘high’ pore volume classes can be encoded as the states  $|0\rangle$  and  $|1\rangle$  of the open wire qubit, respectively.

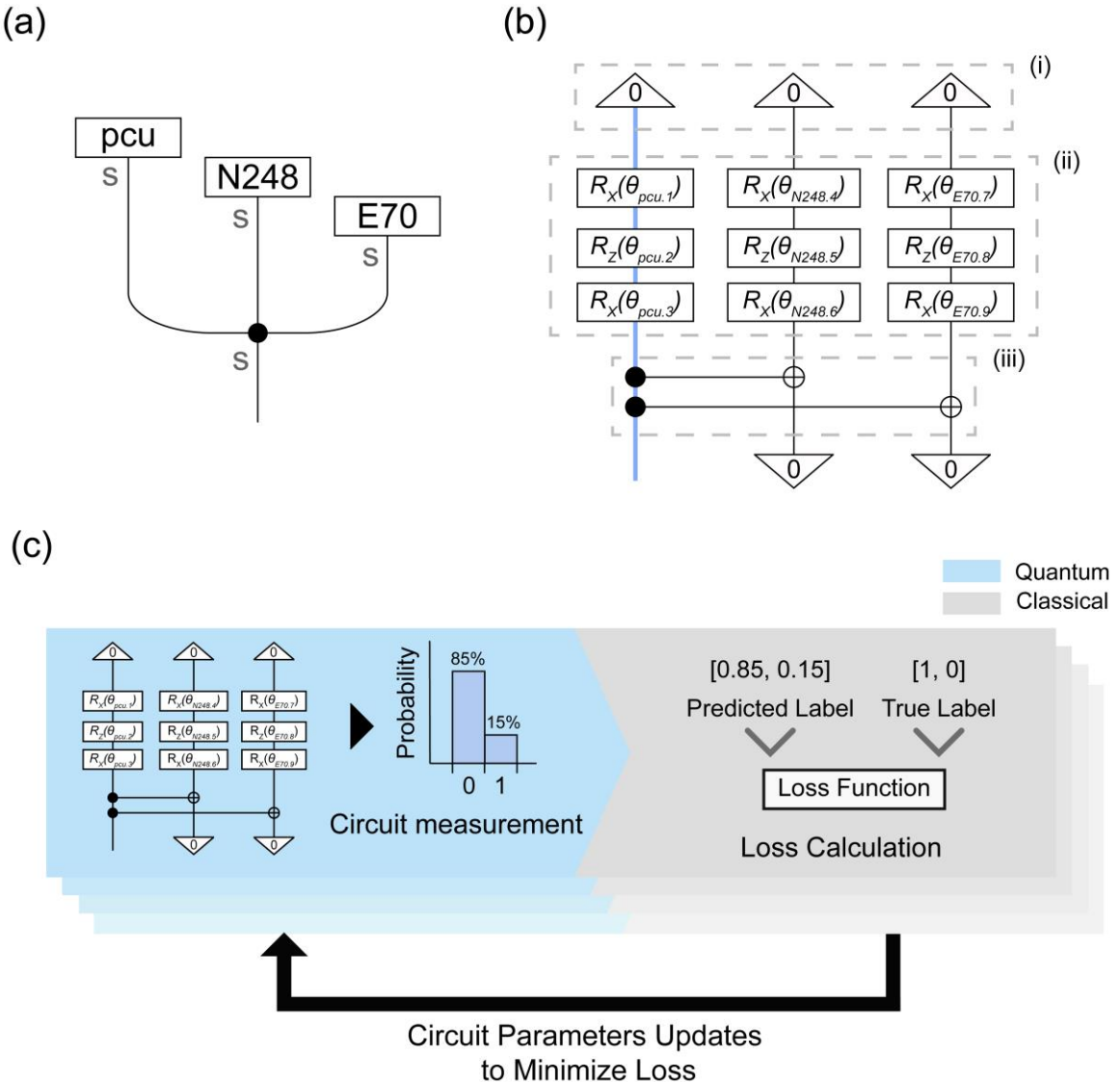


**Figure 3. (a)** String diagrams of MOF representation based on BoW model, and **(b)** its corresponding quantum

circuit with a single-qubit configuration for binary classification based on IQP ansatz. Dotted line boxes represent **(i)** initial quantum states, **(ii)** circuit parameters,  $\theta_{c,n}$ , and **(iii)** controlled-not gates which indicating merge-dot. Open-wire that carries predicted class label is highlighted as blue line. **(c)** An overall process of quantum machine learning.

Once the quantum circuit is constructed based on the choice of QNLP model, the next step is to introduce a quantum machine learning algorithm to optimize the circuit parameters. This optimization ensures that the outcomes from circuit measurements converge to the desired results (i.e. true label, Figure 3c). The output of the quantum circuit is obtained by repeatedly measuring the circuit a specific number of times, known as shots. For instance, in binary classification of pore volume, the measurement outcome is either 0 or 1, where 0 and 1 represent low and high pore volume classes, respectively. These outcomes can be represented as a probability distribution of 0s and 1s as the number of measurements (i.e., shots) accumulates. Initially, the circuit parameters are set at random angles of  $\theta_{c,n} \in [0, 1]$  resulting in the probability distribution that leads to random quantum states. These parameters are fixed based on the component type, although some parameters are shared between quantum circuits corresponding to different MOFs when identical components appear in multiple MOF structures. In total, 78 parameters are used (3 circuit parameters per MOF component which consists of 1 topology, 10 nodes, and 15 edges) for this binary classification task example, and are uniquely combined to represent each MOF. For instance, the circuit parameters for a qubit representing the 'pcu' topology are the same across all MOF structures (e.g., pcu N173 E220, pcu N505 E229, etc.), as only a single topology is considered.

The initial measurement outcome, based on random circuit parameters, often deviate from the desired results, such as 1, assuming the MOF has a high pore volume. Thus, these parameters of the QNLP model (i.e. model weights) are initially set and then iteratively adjusted during training based on stochastic approximation of the gradient derived from the loss function<sup>33</sup> (Figure 3c). This involves a vectorization of the circuit measurement outcomes to match the dimension of the true label, which is represented in one-hot encoding. For instance, binary quantum states  $|0\rangle$  and  $|1\rangle$ , occurring with 85 and 15 shots out of a total of 100 (i.e. probabilities of 85% and 15%), are transformed into the vector  $[0.85, 0.15]$ , and based on which the loss is then calculated. The iterative process, which involves calculating the loss and updating the model's weights, is performed by a classical computer while the measurement of the predicted label is carried out by quantum

computing method. The difference in quantum machine learning over their classical counterpart is that the parameters being optimized,  $\theta_{c,n}$ , are circuit parameters that directly influence the transformation of quantum states, thereby manipulating the probability distribution of the measurement outcomes.

## Comparative Study on QNLP Models

The comparative study was initially conducted to identify the most suitable compositional model for our MOF dataset. For this experiment, the dataset was prepared for the binary classification task (as opposed to multi-class classification task) due to the task complexity and higher computational cost required for the multi-class classification. Therefore, the pore volume of  $1.05 \text{ cm}^3/\text{g}$  and  $\text{H}_2$  uptake of 9.8 weight % were set as the class boundaries for categorizing MOFs with either low or high pore volumes and  $\text{H}_2$  uptakes, respectively. The target classes of low and high were encoded as labels 0 and 1, respectively, to be directly compared with the quantum states (i.e. predicted label) from the circuit measurements. The quantum circuits of MOF were constructed by pre-processing the MOF dataset based on each candidate QNLP models (corresponding to Figures 3b, and S3d, e, f). These circuits were trained to associate MOF names accurately with their corresponding property labels. As mentioned in the previous section, this is achieved by iteratively refining their circuit parameters, which are associated with quantum states to minimize classification errors, as the quantum circuits initially result in random quantum states. Readers are encouraged to refer to the method section for detailed information.

As illustrated in Figure 4, all models exhibited a converging trend over the epochs characterized by decreasing loss, which was subsequently followed by a flattening pattern. For the pore volume dataset (Figure 4a), both word-sequence models showed relatively inferior performance, with their training and validation accuracies not exceeding 80% and a loss of around 0.6. The word-sequence model converged at accuracies of 0.718 and 0.714 and loss of 0.564 and 0.591, and the stair model (i.e., word-sequence with stair model) converged at accuracies of 0.771 and 0.657 and loss of 0.456 and 0.574 for training and validation dataset, respectively. The inferior training performance of sequence-based models was also observed in the  $\text{H}_2$  uptake dataset (Figure 4b). The performance gap between training and validation further increased as losses converged at 0.435 and 0.592 for the word-sequence model and 0.337 and 0.631 for the stair model. Surprisingly, the DisCoCat model showed good convergence behavior, with loss minimized below 0.5 for both datasets. These

outcomes aptly illustrate that MOFs are not sequence-dependent, but rather, they are the aggregate sum of each structural component. Although both DisCoCat and word-sequence models are syntax-sensitive approaches, the rule respecting text order is unsuited to MOF structures. This is because the criterion for completing a MOF structure depends on whether it constitutes a complete set of topology and building blocks rather than the order in which they are listed. This explains the discrepancy in performance between the DisCoCat model and the word-sequence models. The pregroup grammar of DisCoCat is rigidly governed by the syntactic arrangement of the words<sup>12</sup>, whereas the word-sequence models are solely driven by the left-to-right sequence, irrespective of the sentence's components<sup>33</sup>. The best-performing model for our MOF datasets was the bag-of-word model, which illustrates that the modular structure of the MOF dataset is well suited for component-wise multiplication of parsed MOF tensors rather than sequence-based data processing. A similar result was previously reported by Lorenz et al. as the DisCoCat and the BoW models showed comparable performance, while the word-sequence model showed inferior performance for a meaning classification task involving two distinct subjects<sup>33</sup>. Here, the BoW model converged at accuracies of 0.929 and 0.857 for the pore volume training and validation dataset, with the lowest loss among the models as 0.235 and 0.293. The validation accuracy for the H<sub>2</sub> uptake dataset increased to 0.867, with a loss of 0.463. Therefore, the BoW model was chosen as the best candidate to develop the multi-class classification model for pore volumes and H<sub>2</sub> uptakes.

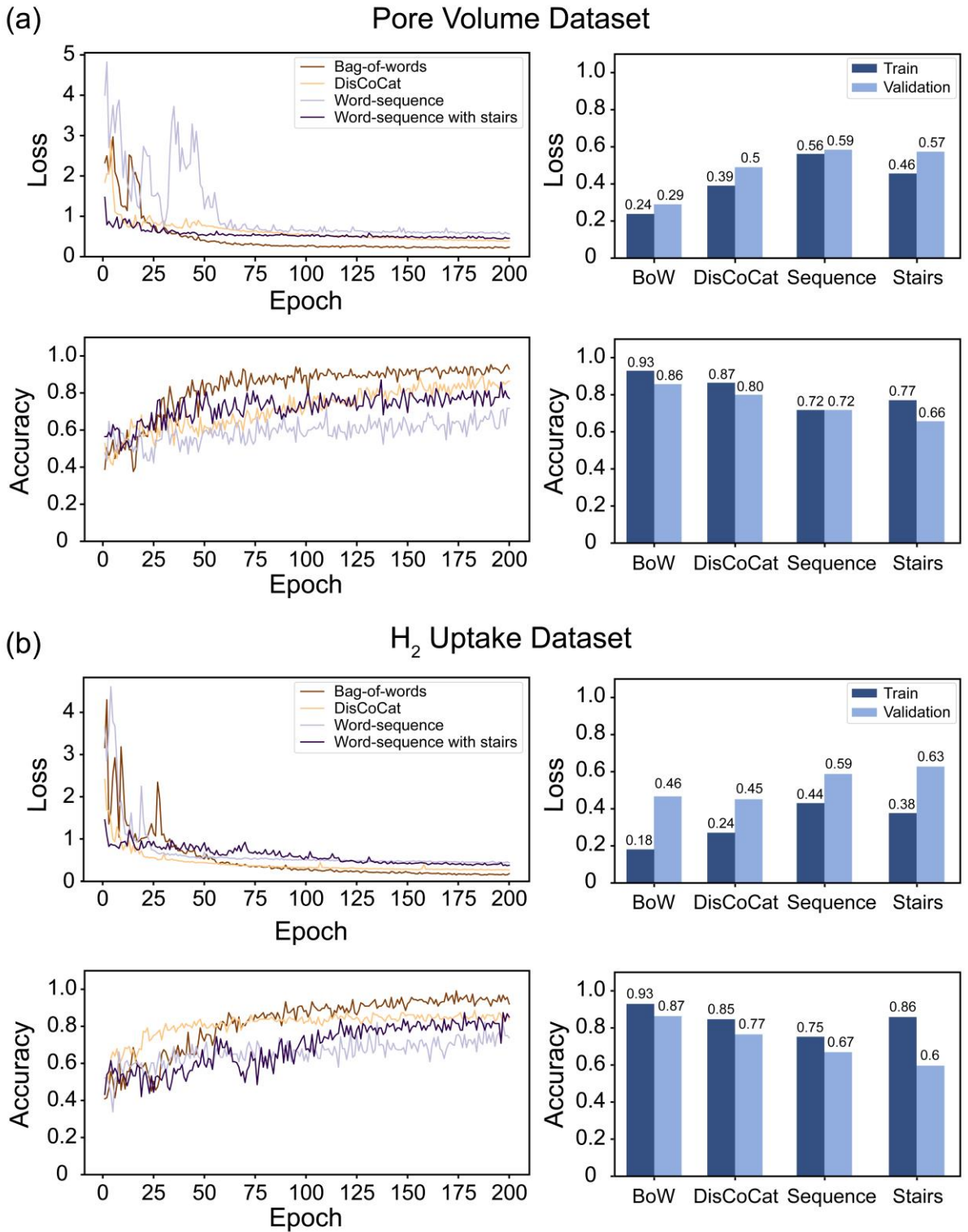


**Figure 4.** Training and validation performance of various model candidates for **(a)** pore volume and **(b)**  $H_2$  uptake binary classification task. The model candidates are the bag-of-words (BoW), distributional compositional categorical (DisCoCat), word-sequence (Sequence), and word-sequence model with stairs (Stairs) models.

## Development of Multi-Class Classification Models based on the Probabilistic Nature of Quantum Machine Learning

In the previous section, MOF structures were assigned 0 or 1 output values based on low/high pore volume/H<sub>2</sub> uptakes. However, in practice, we want more refined categories for classifications (e.g. very high pore volume, high pore volume, average pore volume, low pore volume), especially for inverse design purposes. Thus, the transition from binary classification to multi-class classification is important for practical purposes. Accordingly, the MOF datasets divided into four classes (low/moderately low/moderately high/high) were transformed into quantum circuits for multi-classification applications based on the choice of data representation schemes, the BoW model from the previous section (Figure 5a). The fundamental difference between the circuit construction for binary and multi-classification is the number of qubits required to represent the MOFs, which leads to a difference in the probability of obtaining meaningful outcomes. The output of the quantum circuit is delivered by a specific number of qubits. For example, a quantum circuit of MOF representation for binary classification requires a single output qubit to deliver the probability distribution of predicted labels of 0 and 1 while that for the multi-classification requires two output qubits to represent the probability distribution of predicted labels of 00, 01, 10, and 11. Thus, the QNLP model involves a post-processing step known as post-selection, which retains only the measurement outcomes related to the predicted class label and filters out the remaining measurements based on a specific quantum state, 0-effect<sup>33</sup>. The term, 0-effect, is used as it determines whether to keep or discard the measurement outcomes based on whether the state of the post-selected qubits matches the computational basis state, |0⟩. For instance, in a binary classification task implemented with a quantum circuit using three qubits to encode possible classes, post-selection is used to consider only those states where both second and third qubits are in the |0⟩ state, such as |000⟩ and |100⟩. This selective measurement filters out results where the post-selected qubits are |1⟩ (i.e., states |011⟩ or |110⟩), thus focusing the analysis on the relevant subset of the quantum state space. That is, the post-selection is to measure all quantum states but only interpret the state of the open-wire qubits for final classification, considering the states of the other qubits as ancillary information that supports the coherence of the quantum states but isn't directly used for decision-making.

In the MOF representation for binary classification, as discussed previously, each MOF is assigned a binary label 0 (i.e. low) or 1 (i.e. high) depending on their pore volume or H<sub>2</sub> uptake properties. The assigned label becomes the true label compared with the predicted label as a result of the circuit measurement. This

requires the post-selection on  $|0\rangle$  state of the two qubits to retain meaningful quantum states ( $|000\rangle$  and  $|100\rangle$ ) from the total probability distribution resulting from the circuit measurements. For example, the quantum circuit based on BoW model for binary classification allocates a single qubit for each MOF component vector (i.e., topology, node, and edge). This results in a total of 3 qubits, allowing  $2^3$  possible quantum states, from 000 to 111 (Figure 5b). Since the measurement outcome needs to be converged into single qubit states of 0 and 1, the measurement outcomes of 000 and 100 are interpreted as the probability distribution of predicted labels of 0 and 1, respectively. Based on the post-selection criterion, the remaining measurement outcomes are discarded. This indicates that assuming all possible outcomes have a uniform distribution (e.g. all  $2^3$  quantum states are observed 125 shots each when measuring the circuit 1000 shots), only two in  $2^3$  shots would result in a meaningful outcome representing the probability distribution of predicted labels (Figure 5b). The prediction accuracy and loss are then calculated based on these post-selected outcomes.

The MOF representation for the multi-class classification, on the other hand, further increases the number of post-selections as it necessitates at least two open-wire qubits to represent the assigned label. Four classes of low, moderately low, moderately high, and high are encoded into two-qubit configurations of 00, 01, 10, and 11, and then compared with the resulting probability distribution. As mentioned in the previous section, the output of the BoW model is represented as a n-dimensional single tensor, derived from the component-wise multiplication of n component vectors. For instance,  $n = 3$  to represent a single MOF for binary classification, as it consists of three components of topology, node, and edge. This component-wise multiplication is encoded into the quantum circuit by entangling individual component qubits with an open wire qubit using controlled-not operations, representing the merge-dot of the string diagram (Figure 3b(iii)). Thus, for the multi-classification task, two open wire qubits are required to deliver quaternary quantum states, necessitating the duplication of required qubits by  $n$  (Figure 5a). This enables the comparison with true labels encoded as a two-qubit configuration but further increases statistical limitations by requiring the post-selecting of 4 qubits (Figure 5c). That is, four in  $2^6$  shots would yield meaningful results, assuming the uniform distribution of total outcomes, and this notably reduces statistical significance by a factor of 4 compared to the binary classification situation. The number of post-selections required grows exponentially as the number of classes increases. This indicates that the number of circuit measurements (i.e. shots) also needs to increase exponentially in accordance with the number of post-selections to obtain meaningful statistics. To address this issue, the number of circuit executions for binary and multi-class classification models discussed in this section is set at 2048 and 8192 shots,

respectively.

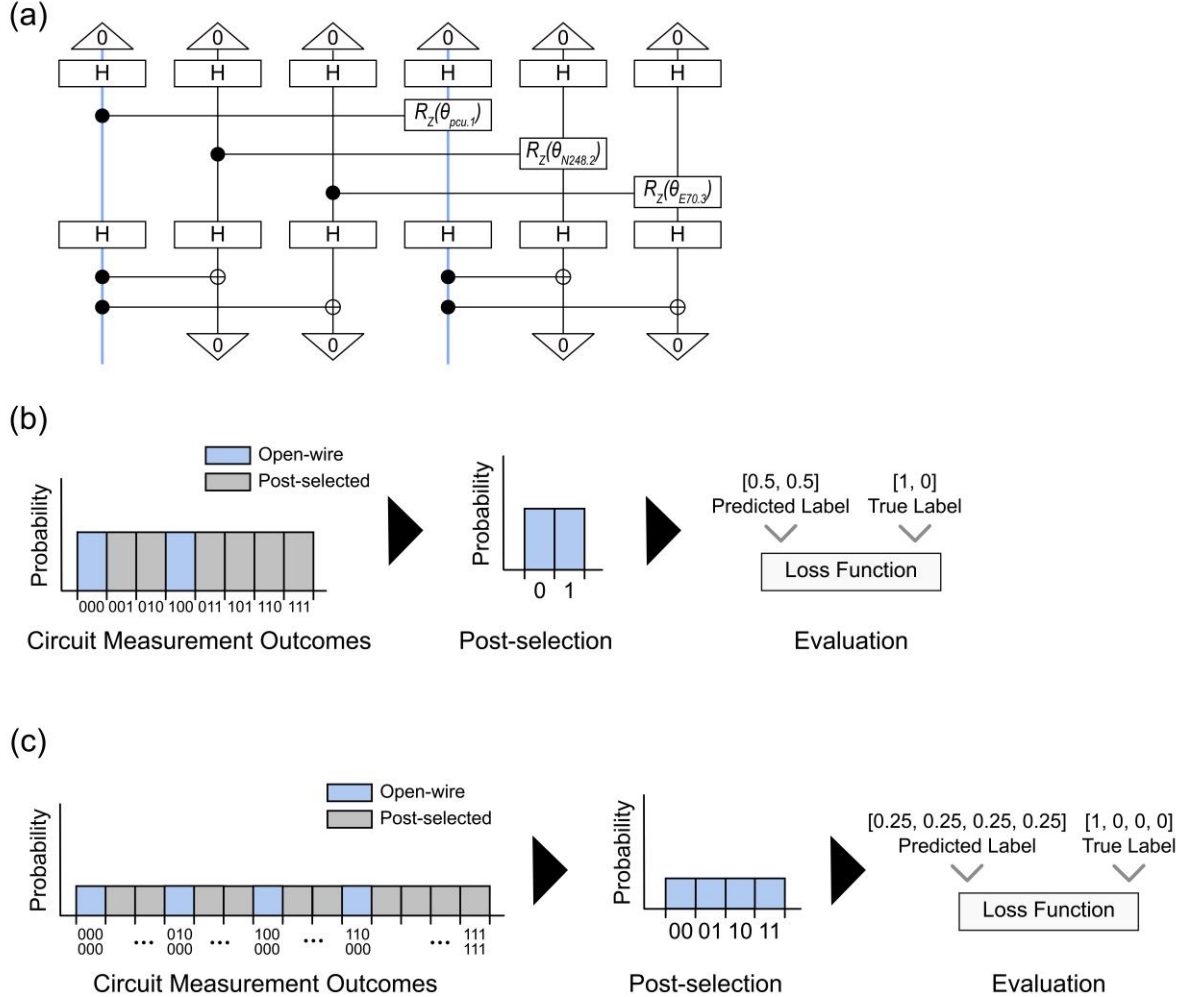


**Figure 5. (a)** Quantum circuits of MOF named pcu N248 E70 with two-qubit configuration for multi-classification tasks. Note that the blue lines represent open wires, and rectangles pointing downward represent qubits with a 0-effect. **(b)** A post-selection process assuming the quantum circuit measurement result in a uniform distribution for binary classification and **(c)** multi-classification tasks. The circuit measurement outcomes after the post-selection is vectorized to be matched with one-hot encoding form of the true labels.

In addition to the difference in qubit requirements, the limited sample size per class makes model training for multi-class datasets difficult. Splitting the datasets with binary labels results in 75 samples per class, while the datasets with multi-class labels result in 37 or 38 samples per class out of a total of 150 samples.

Therefore, the task complexity of training models for datasets with multi-class labels is much higher than that with binary labels as illustrated in Figure S5. One way to circumvent the limitation without increasing the overall dataset size or circuit depth is to transform the multi-class datasets into binary label-like datasets by separating them in a 20:80 ratio. For example, BoW model can be trained for binary classification based on the dataset divided into 38 samples of ‘low’ class with label 0 and the rest of the 112 samples labeled with 1. Similarly, 37 samples of ‘moderately low’ class would be labeled as 0, and the rest of the 113 samples would be labeled as 1; therefore, the trained BoW model becomes a 01-specialized model. Based on this strategy, the required qubits per MOF data point are maintained at three qubits; therefore, the number of circuit executions to obtain meaningful results for each class can be kept as 25 % of implementing the single multi-classification model. Figure 6 illustrates training results of the four BoW models based on 00, 01, 10, and 11-specialized datasets. The training history showed good convergence behavior with smooth exponential decay, similar to that of the 50:50 binary dataset (Figure 4), while the multi-class datasets showed large fluctuations over epochs (Figures 6a, b). The prediction accuracies showed consistent results with significant difference between multi-class and class-specialized datasets (Figures 6c, d). The single multi-classification model showed inferior performance over individual binary classification models trained on each class-specialized dataset by showing the average percent differences of 55.9% and 51.4% for the pore volume and H<sub>2</sub> uptake, respectively. Consequentially, these results reflected increased task complexity in the multi-class datasets, which were caused by changes in trainable sample size.

Among BoW models for binary classification, a unique U-shaped trend was observed in the accuracy for both pore volume and H<sub>2</sub> uptake as the values started at about 0.9 in 00, reached the minimum value in 01, and then recovered in 11-specialized datasets. This is mainly because the overall trend of the building block dependency is focused on the low and high-class datasets, and the moderately low-class datasets have the least number of class-significant building blocks (Figure 2b, d). However, the important point is that the validation and test accuracies showed superior performance compared to that of a single model trained on the multi-class datasets, resulting in accuracies all above 0.7 (Figures 6c, b). Despite the trade-off of training multiple models, the author believes this approach is a reasonable solution to maintaining dataset size and the complexity of the quantum model, considering the quantum resource in the NISQ device. Thus, this multi-QNLP model-based architecture was adopted to further experiment with the MOF generation task.

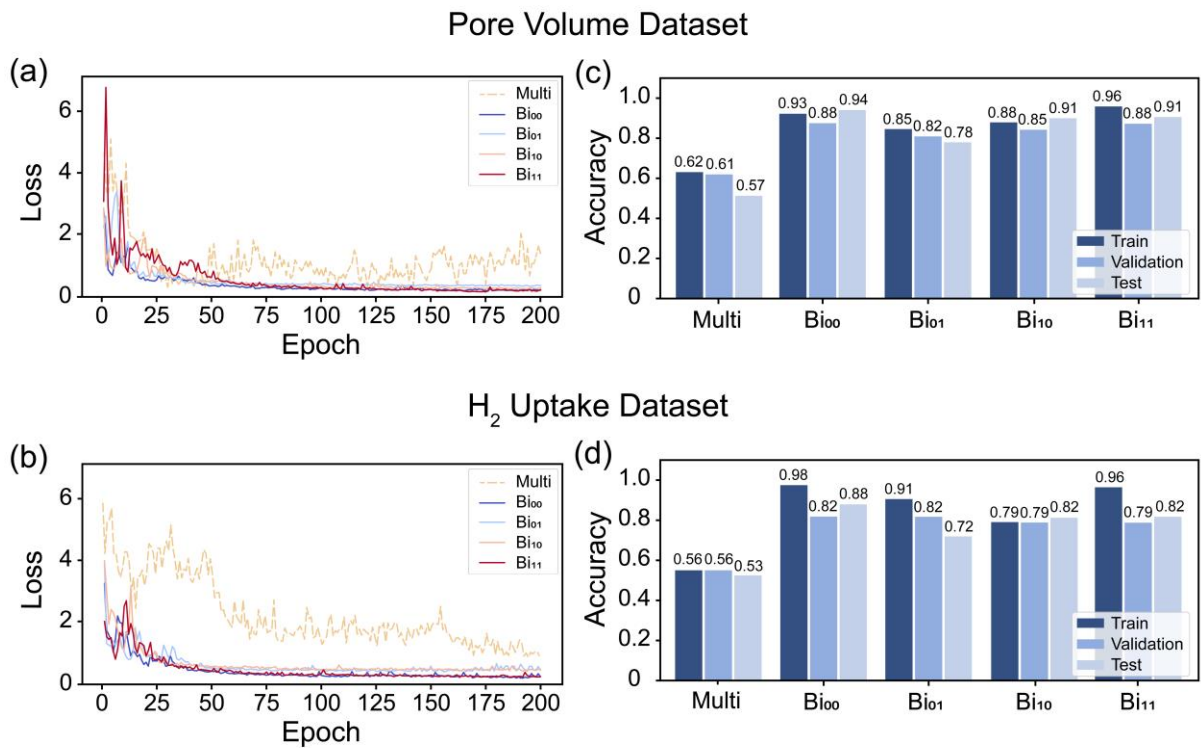


**Figure 6.** Training history of loss based on (a) pore volume and (b) H<sub>2</sub> uptake dataset. Accuracy bar graphs of (c) pore volume and (d) H<sub>2</sub> uptake datasets. Note that Multi, Bi<sub>00</sub>, Bi<sub>01</sub>, Bi<sub>10</sub>, and Bi<sub>11</sub> represent BoW models trained based on the multi-classification dataset, 00-specialized dataset (binary classification dataset divided into classes 00 and 01+10+11), 01, 10, and 11-specialized datasets, respectively.

## Inverse Design of MOFs with Target Property

As sentences are considered logically correct based on word choice and grammar, MOFs can be defined as complete when they are satisfied with the necessary components and ‘MOF’ grammar. Naturally, there are three necessary components to complete a single MOF: topology, node, and edge. However, we need to define which generation rule to apply to generate complete MOFs, so the MOF grammar should be introduced similarly to the role of grammar in sentences. The MOF grammar in this study followed two simple rules: 1) the MOF components listed in order of topology, node, and edge names to be matched with the true dataset and 2) only a single combination between the building blocks is allowed (i.e., No mixed metal or mixed ligand form is allowed such as “pcu N123 N106 E70”). Based on these simple rules, a MOF generation loop was developed as a role of input generation for the classification models on pore volumes and H<sub>2</sub> uptakes

(Figure 7a).

Once the text-based MOF input data is generated, it is transformed into the quantum circuit based on the BoW string diagram. Then, the quantum classification models discussed in the previous section evaluate the input MOF's property based on the probability distribution obtained from the circuit measurements (Figure 7b). A single MOF quantum circuit is used as an input for four distinct classification models: Model 00 (i.e., BoW models trained on datasets specialized for label '00'), Model 01, Model 10, and Model 11. The interpretation of total probability distributions from these four models is based on the relative probability distributions against a class label '0', as each model is specialized to recognize a specific range of properties. Here, the label '0' represents specialized property classes (i.e., low, moderately low, moderately high, and high) which corresponds to quantum state '0' from the classification models. For instance, if the '0' state (i.e. specialized property class) of the MOF quantum circuit is measured with probabilities of 5%, 1%, 3% and 95% in the H<sub>2</sub> uptake models 00, 01, 10, and 11, respectively, the MOF is likely to have a high H<sub>2</sub> uptake with 91.3% relative probability (Figure 7b). Finally, the MOF is evaluated to determine if it possesses the desired property, based on whether the highest relative probability exceeds a set threshold. In this study, the threshold probability was set at 85%. The MOF that meets the threshold goes through the structure generation process, while those that do not are redirected back to the input generation stage. This cycle continues until a generated MOF satisfies the threshold condition. The structure generation process based on the MOF text input is done by classical computation based on our in-house software, PORMAKE<sup>35</sup> (Figure 7c). The MOF name's raw text generated in step 1 (e.g., pcu N123 E9) can be directly inputted, as it adheres to the naming convention of building blocks used in PORMAKE.

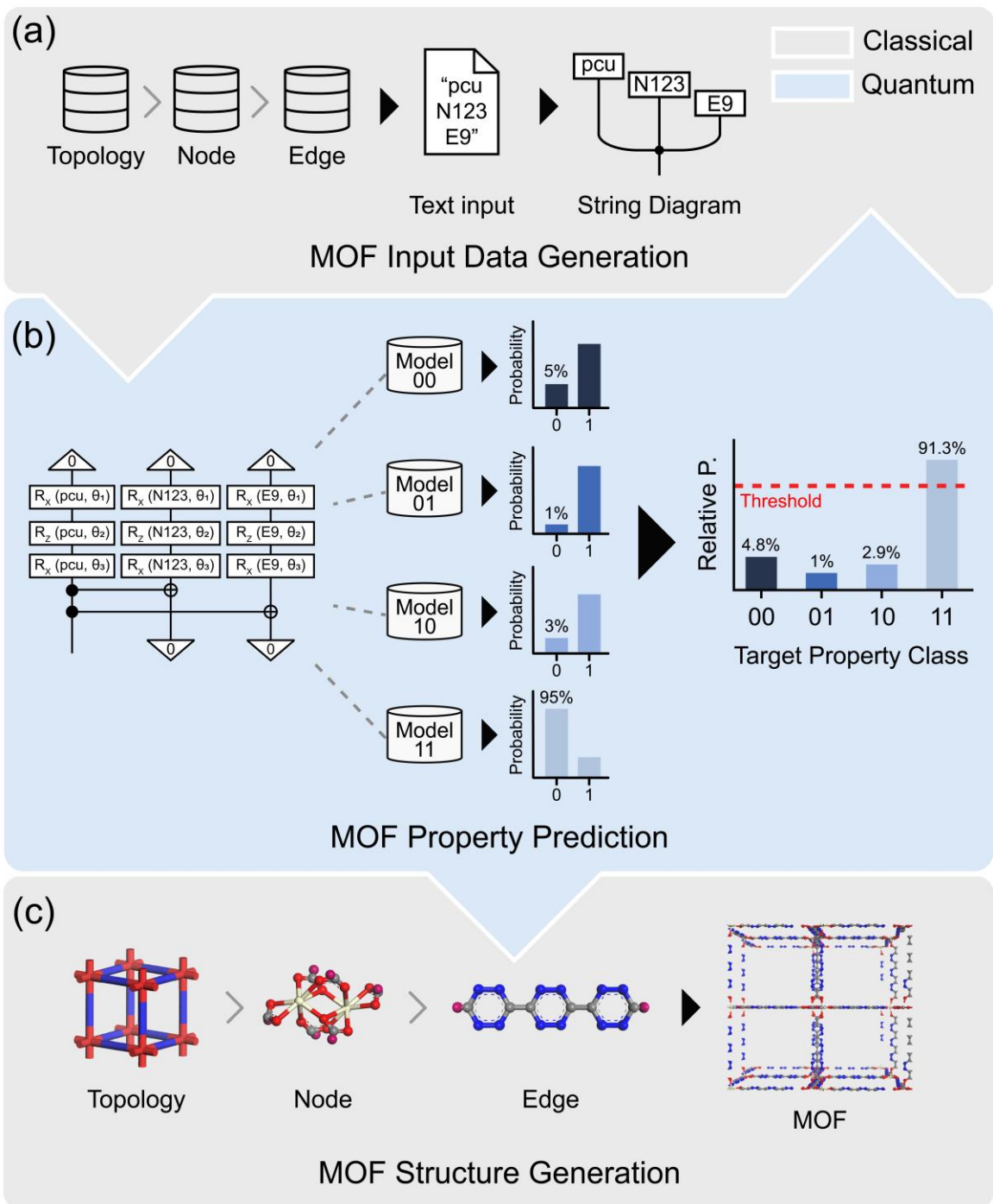


**Figure 7.** The overall workflow of the MOF generation process: **(a)** MOF input generation process based on random selection rule. **(b)** Property prediction based on relative probability distributions collected from four binary classification models. **(c)** MOF structure generation based on selected building blocks.

The resulting MOF generation framework showed good performance, with a total average accuracy of

91.25% (Table 1). The overall generation performance improved by 6.5% compared to the classification performance, which exhibited a descending trend from low to high property classes. This contrasts with the U-shaped trend observed in the classification models (Figure 6), which can be attributed to the influence of other models' performance. The evaluation of the MOF generation task is based on comprehensive contribution of each model's performance, whereas the classification performance is solely driven by the individual performance of the classification models. For instance, the relative probability of the least performing classification model, Model 01, benefits from the contributions of Models 00, 10, and 11. This collaborative approach enables it to more accurately identify MOF inputs by increasing its relative probability of making correct predictions, as Models 00, 10, and 11 yield low probabilities against the label '0' when the MOF input has a 'relatively low' class, and vice versa. On the other hand, the best-performing model, Model 00, risks its accuracy by incorporating predictions from Models 01, 10, and 11, which are relatively less accurate. In fact, the performance across target classes showed the largest average improvement in the 'relatively low' class, with an increase of 18.5%, while the 'high' class showed only a 0.5% average improvement.

The average number of guesses until correct prediction can be interpreted as a metric that distinguishes between incorrect predictions and timeouts. A timeout occurs when the QNLP models' predictions reach 100 trials without achieving a prediction that satisfies the 85% threshold probability. As the number of timeout trials increases, so does the average number of guesses, conveying a meaning slightly different from that of an incorrect prediction. An incorrect guess indicates the model's failure to accurately predict a MOF's property, while a timeout suggests that the model has not yet delivered its prediction, retaining the potential to eventually make correct predictions. This distinction allows for a comprehensive evaluation of the generation performance across target classes beyond merely assessing accuracy. Specifically, in the H<sub>2</sub> uptake dataset, the 'high' class achieved 82% accuracy with an average of 30.75 guesses, whereas the 'moderately high' class in the pore volume dataset reached 86% accuracy with an average of 15.09 guesses (Table 1). When solely evaluating performance based on accuracy, the generation performance of the 'high' case might appear inferior to that of the 'moderately high' case. However, the 'high' case included 5 timeouts, while the 'moderately high' case had none, meaning all 14 trials not included in the accuracy calculation were incorrect predictions (Table S1). As a result, our MOF generation framework of the multi-model-based architecture showed outstanding performance across target properties with an average accuracy of 93.5% and 89% for pore volume and H<sub>2</sub> uptake, respectively. The structure generation process was not discussed since it falls beyond the scope of this paper, but

some of the generated MOF structures are provided in Figure S6. Structure files of 150 MOFs were also provided in Crystallographic Information Framework (.cif) form.

**Table 1.** The test result of generating MOF with target property. The accuracy was calculated as the ratio of correct predictions over a total of 100 generation tasks (the number of correct, incorrect, and timeouts was considered).

Target Property	Pore Volume		H <sub>2</sub> Uptake	
	Accuracy [%]	Avg. Guess	Accuracy	Avg. Guess
Low	100	9.03	93	20.33
Mod. Low	96	26.56	91	17.68
Mod. High	86	15.09	90	37.8
High	92	22.79	82	30.75

## Extensibility of QNLP to Complex Reticular Frameworks

Although our simple MOF dataset of fixed topology with a single building block combination resulted in a non-sequence and non-syntax-sensitive model as the optimum approach (i.e. BoW model), the authors want to highlight that this result doesn't capture the complexity inherent in MOF structures. For example, two mixed-metal MOFs with identical chemical compositions but different arrangements of the guest metal clusters can be identified as different structures because the spatial arrangement of the components can affect their chemical properties<sup>36</sup>. In fact, the sequence is one of the key parameters often introduced to compositionally repeating structures for structural representation and analysis. That is, the sequence of the materials becomes the boundary of determining whether they are identical or not. For example, Phong et al. addressed the periodicity of the block copolymers as a factor causing a difference in mechanical and thermal phase behavior<sup>37</sup>. They synthesized two types of dynamic block copolymers (DBCPs) with identical chemical compositions of PEG and PDMS oligomers but different sequences. Despite their identical chemical composition, well-ordered periodic DBCPs exhibited higher ionic conductivity and flow temperature than DBCPs with random sequences, which were attributed to the enhanced ion-transporting and thermal stability due to the formation of supramolecular nanofibers by stacking the hydrogen bonding units<sup>37</sup>. Another familiar example is DNA sequence. The sequence of DNA block copolymers was proved to play a crucial role in dictating the physical form and properties of the

assembled structures as variations in the DNA sequences led to the formation of three distinctly different structures by Rizzuto et al<sup>38</sup>.

As mentioned earlier, this concept is applicable to many other periodic crystalline materials, such as MOFs and covalent organic frameworks (COFs). Recently, Canossa et al. claimed the concept of sequence as one of the crucial indicators for defining structural identity and distinctive properties of multivariate crystals<sup>39</sup>. They defined this sequential property as unit cell information capacity (UCiC) to store tunable chemical or physical information of multivariate frameworks<sup>39</sup>. When a material has the number of  $n$  tunable variables and  $m_i$  is the multiplicity of  $i^{th}$  variable, UCiC is defined as:

$$\text{UCiC} = \prod_{i=1}^n m_i = m_1 \times m_2 \times \dots \times m_n \quad (1)$$

As UCiC is a highly flexible variable contingent upon the framework's defined variables and variants, the optimal model for material representation also greatly depends on the complexity of the periodic structures. Consequently, the four compositional models we studied for representing simple MOF structures necessitate careful selection and further refinement based on the target materials. Thus, the extensibility of QNLP to other complex materials would depend on how well the algorithm respects the structural identity of the materials while addressing the statistical challenges from the increased requirement for qubits to process such complexities.

## Conclusion

In this study, we experimented with the applicability of quantum natural language processing for the inverse design of the MOFs with the desired target properties of pore volume and H<sub>2</sub> uptake. The target properties of pore volume and H<sub>2</sub> uptake were calculated against 150 hypothetical MOF structures consisting of a pcu topology, 10 metal nodes, and 15 organic edges. To construct a multi-class classification model, these datasets were evenly separated into four classes: low, moderately low, moderately high, and high classes for pore volume and H<sub>2</sub> uptake, respectively. A comparative study of pre-existing QNLP models was conducted to find an optimum approach to process quantum circuits in our MOF dataset. The results showed the best performance in the following order: BoW, DisCoCat, and sequence-based models, with the top-performing

model achieving validation accuracies of 85.7% and 86.7% for binary classification based on the pore volume and H<sub>2</sub> uptake datasets, respectively. This performance is attributed to the non-sequence-dependent nature of our MOF datasets, meaning that completing a MOF structure relies on whether it includes a complete set of topology and building blocks rather than the order in which they are assembled. Based on the choice of the QNLP model, multi-class classification models were developed, considering the probabilistic nature of quantum circuit measurements. Four binary classification models were individually optimized to the specific target classes, and the models showed test accuracies of 93.9%, 78.1%, 90.6%, and 90.9% for low, moderately low, moderately high and high pore volume classes, respectively. Similarly, the test accuracies on the H<sub>2</sub> uptake dataset recorded 87.9%, 71.9%, 81.2%, and 81.8%. The performance of generating MOFs with desired properties showed improved accuracies by 6.5% on average owing to the requirements in the generation framework that the classification models exceed the confidence threshold of 90%.

The extensibility of QNLP to other materials was further discussed based on the significance of sequence in effectively describing the complex nature inherent in the periodic materials. The comparative study presented in this paper was limited to the simple MOF structures, where the arrangement and sequence of components were considered less critical. However, this should not imply that all MOF data should be treated without regard to sequence. In fact, the complexity of many periodic materials necessitates careful design that considers sequence as a key factor in defining structural identity<sup>39</sup>. This leads us to believe that the effectiveness of QNLP in material science depends on its ability to deal with the detailed structures of the materials. Although our study only looked at a small part of the wide variety of MOF search spaces, we believe applying QNLP to design MOFs with a limited dataset is an exciting first step. Our approach, inspired by successful applications of QNLP in fields as diverse as sentence generation<sup>14</sup> and music composition<sup>15</sup>, demonstrated the potential for classifying and generating large periodic materials with desired properties. This method could provide a novel perspective on efficiently navigating the vast search space of MOFs by bridging the gap between quantum algorithm and material design.

## Methods

### Dataset Preparation

The MOF structures for the quantum model training were generated using our in-house software, PORMAKE<sup>35</sup>. These 150 hypothetical MOF structures were optimized by applying a force field in BIOBIA Materials Studio 2019<sup>40</sup>. The target geometrical property, pore volume, was calculated based on a channel and probe radius of 1.2 and the number of Monte Carlo samples per unit cell of 5000 using Zeo++<sup>41</sup>. Target chemical property, H<sub>2</sub> uptake, of 150 MOFs was calculated at 77 K and 100 bar using the RASPA package<sup>42</sup>. UFF was used for MOF structures with the Lorentz-Berthelot mixing rule and a cutoff distance of 12.8 Å. H<sub>2</sub> molecules were represented with a united atom model, and a pseudo-Feynman-Hibbs model was applied to reflect the behavior of the H<sub>2</sub> gas at low-temperature conditions<sup>43</sup>. Therefore, Lenard-Jones 12-6 potentials were fitted to the Feynman-Hibbs potential. GCMC simulations were performed for 5,000 initialization cycles and 10,000 production cycles. Then, boundaries for class labels were determined based on 25, 50, and 75 percentiles of target properties' distributions (Figure 2). Train, validation, and test datasets were divided into 85, 35, and 30 samples.

## Quantum Model Training

The MOF input data was processed for quantum computation using lambeq, an open-source Python library for QNLP<sup>44</sup>. The input data consisted of a class label and its corresponding MOF name in order of topology, node, and edge (SI 2). The difference between NLP and QNLP starts from the input data processing, while their goal remains the same: translation between unstructured and structured language. To prepare the quantum circuits representing instructions of the gate operations to encode MOF information in qubits, the dataset was first tokenized and processed into the string diagrams based on the choice of the models: bag-of-word, DisCoCat, and word-sequence models. The four types of method were used to generate the string diagrams as shown in Figure 5. The DisCoCat model-based approach necessitates the conversion of pregroup diagrams into string diagrams; accordingly, the dataset underwent processing based on rewriting rules<sup>33</sup>. The string diagrams, representing MOF data, were subsequently transformed into quantum circuits employing the IQP (Instantaneous Quantum Polynomial) ansatz with the choice of two Rx gates and a single Rz gate. Although the specific selection of the ansatz should not be overly emphasized<sup>33</sup>, the IQP was chosen due to its well-reported accomplishments in prior research<sup>14, 15, 33, 45</sup>. The single IQP layer was used throughout the experiments to maintain the circuit depth small. All QNLP models studied in this paper were trained using simulated

hardware based on Qiskit AerBackend<sup>27</sup> with 8192 shots (2048 shots for binary models 00 to 11). In addition, all models were trained on a cross-entropy objective, and the quantum parameters were updated based on the Simultaneous Perturbation Stochastic Approximation (SPSA) optimization method<sup>46</sup>. The initial learning rate and initial parameter shift scaling factor were set as 0.05 and 0.06, respectively, while the stability constant of the classical optimizer were uniquely chosen for each model based on the tuning test (Table S2).

## MOF Text Input Generation Algorithm

The generation algorithm was implemented with context-free grammar (CFG) using the natural language toolkit<sup>47</sup>. The CFG for MOFs was designed to adhere to a random generation rule. Individual MOF building blocks were randomly selected from the search space for topology, nodes, and edges, respectively.

## MOF Generation Test

The MOF generation performance was measured based on 100 individual tests for each class. The accuracy of generating MOF with the target class was calculated based on the ratio of correct guesses against total guesses. Total guesses were defined as a sum of time-out, correct, and incorrect guesses (i.e. 100 runs). The time-out indicates a situation in which the QNLP model's prediction exceeds 100 iterations to output a prediction satisfying a threshold probability of 85%.

## **Conflicts of Interest**

The authors declare no competing financial interest.

## **Code availability**

Code for MOF QNLP model training and MOF generation is available at

[https://github.com/shinyoung3/MOF\\_QNLP](https://github.com/shinyoung3/MOF_QNLP)

## **Author Information**

### **Corresponding Author**

\*Jihan Kim – Department of Chemical and Biomolecular Engineering, Korea Advanced Institute of Science and Technology (KAIST), E-mail: jihankim@kaist.ac.kr

### **Present Addresses**

Shinyoung Kang: Korea Advanced Institute of Science and Technology, Daejeon, 34141, Republic of Korea

Jihan Kim: Korea Advanced Institute of Science and Technology, Daejeon, 34141, Republic of Korea

### **Author Contributions**

S.K. performed the calculation, analysis and writing of the manuscript and J.K. supervised the project. All authors read and approved the manuscript.

## **Acknowledgment**

We thank National Research Foundation of Korea (Project Number RS-2024-00337004) for the financial support.

## References

(1) Feynman, R. P. Simulating Physics with Computers. *International Journal of Theoretical Physics* **1982**, *21*, 467.

(2) Sajjan, M.; Sureshbabu, S. H.; Kais, S. Quantum Machine-Learning for Eigenstate Filtration in Two-Dimensional Materials. *J Am Chem Soc* **2021**, *143* (44), 18426-18445. DOI: 10.1021/jacs.1c06246 From NLM PubMed-not-MEDLINE.

(3) Sajjan, M.; Li, J.; Selvarajan, R.; Sureshbabu, S. H.; Kale, S. S.; Gupta, R.; Singh, V.; Kais, S. Quantum machine learning for chemistry and physics. *Chem Soc Rev* **2022**, *51* (15), 6475-6573. DOI: 10.1039/d2cs00203e From NLM Medline.

(4) Biamonte, J.; Wittek, P.; Pancotti, N.; Rebentrost, P.; Wiebe, N.; Lloyd, S. Quantum machine learning. *Nature* **2017**, *549* (7671), 195-202. DOI: 10.1038/nature23474.

(5) Preskil, J. Quantum Computing in the NISQ era and beyond. *Quantum* **2018**, *2*, 79.

(6) Andersson, M. P.; Jones, M. N.; Mikkelsen, K. V.; You, F.; Mansouri, S. S. Quantum computing for chemical and biomolecular product design. *Current Opinion in Chemical Engineering* **2022**, *36*. DOI: 10.1016/j.coche.2021.100754.

(7) Kanno, S.; Tada, T. Many-body calculations for periodic materials via restricted Boltzmann machine-based VQE. *Quantum Science and Technology* **2021**, *6* (2). DOI: 10.1088/2058-9565/abe139.

(8) Brown, P.; Zhuang, H. Quantum machine-learning phase prediction of high-entropy alloys. *Materials Today* **2023**, *63*, 18-31. DOI: 10.1016/j.mattod.2023.02.014.

(9) Naseri, M.; Gusarov, S.; Salahub, D. R. Quantum Machine Learning in Materials Prediction: A Case Study on ABO(3) Perovskite Structures. *J Phys Chem Lett* **2023**, *14* (31), 6940-6947. DOI: 10.1021/acs.jpclett.3c01703 From NLM PubMed-not-MEDLINE.

(10) Mathematical Foundations for a Compositional Distributional Model of Meaning. *ArXiv* **2010**.

(11) Ruskanda, F. Z.; Abiwardani, M. R.; Syafalni, I.; Larasati, H. T.; Mulyawan, R. Simple Sentiment Analysis Ansatz for Sentiment Classification in Quantum Natural Language Processing. *IEEE Access* **2023**, *11*, 120612-120627. DOI: 10.1109/access.2023.3327873.

(12) Zeng, W.; Coecke, B. Quantum Algorithms for Compositional Natural Language Processing. *Electronic Proceedings in Theoretical Computer Science* **2016**, *221*, 67-75. DOI: 10.4204/ptcs.221.8.

(13) Cerezo, M.; Verdon, G.; Huang, H. Y.; Cincio, L.; Coles, P. J. Challenges and opportunities in quantum machine learning. *Nat Comput Sci* **2022**, *2* (9), 567-576. DOI: 10.1038/s43588-022-00311-3 From NLM Medline.

(14) Amin Karamlou, M. P., James Wootton. Quantum Natural Language Generation on Near-Term Devices. *arXiv* **2022**. DOI: arXiv:2211.00727v1

(15) Eduardo Reck Miranda, R. Y., Anna Pearson, Konstantinos Meichanetzidis, Bob Coecke. A Quantum Natural Language Processing Approach to Musical Intelligence. *arXiv* **2021**. DOI: arXiv:2111.06741v2.

(16) Furukawa, H.; Cordova, K. E.; O'Keeffe, M.; Yaghi, O. M. The chemistry and applications of metal-organic frameworks. *Science* **2013**, *341* (6149), 1230444. DOI: 10.1126/science.1230444.

(17) Wang, M.; Dong, R.; Feng, X. Two-dimensional conjugated metal-organic frameworks (2D c-MOFs): chemistry and function for MOFtronics. *Chem Soc Rev* **2021**, *50* (4), 2764-2793. DOI: 10.1039/d0cs01160f.

(18) Feng, L.; Day, G. S.; Wang, K.-Y.; Yuan, S.; Zhou, H.-C. Strategies for Pore Engineering in Zirconium Metal-Organic Frameworks. *Chem* **2020**, *6* (11), 2902-2923. DOI: 10.1016/j.chempr.2020.09.010.

(19) Meng, S. S.; Xu, M.; Guan, H.; Chen, C.; Cai, P.; Dong, B.; Tan, W. S.; Gu, Y. H.; Tang, W. Q.; Xie, L. G.; et al. Anisotropic flexibility and rigidification in a TPE-based Zr-MOFs with scu topology. *Nat Commun* **2023**, *14* (1), 5347. DOI: 10.1038/s41467-023-41055-6 From NLM PubMed-not-MEDLINE.

(20) Smith, M. K.; Jensen, K. E.; Pivak, P. A.; Mirica, K. A. Direct Self-Assembly of Conductive Nanorods of Metal-Organic Frameworks into Chemiresistive Devices on Shrinkable Polymer Films. *Chemistry of Materials* **2016**, *28* (15), 5264-5268. DOI: 10.1021/acs.chemmater.6b02528.

(21) Suresh, K.; Matzger, A. J. Enhanced Drug Delivery by Dissolution of Amorphous Drug Encapsulated in a Water Unstable Metal-Organic Framework (MOF). *Angew Chem Int Ed Engl* **2019**, *58* (47), 16790-16794. DOI: 10.1002/anie.201907652 From NLM Medline.

(22) Chen, Z.; Mian, M. R.; Lee, S. J.; Chen, H.; Zhang, X.; Kirlikovali, K. O.; Shulda, S.; Melix, P.; Rosen, A. S.; Parilla, P. A.; et al. Fine-Tuning a Robust Metal-Organic Framework toward Enhanced Clean Energy Gas Storage. *J Am Chem Soc* **2021**, *143* (45), 18838-18843. DOI: 10.1021/jacs.1c08749 From NLM PubMed-not-MEDLINE.

(23) Rodenas, T.; Luz, I.; Prieto, G.; Seoane, B.; Miro, H.; Corma, A.; Kapteijn, F.; Llabres, I. X. F. X.; Gascon, J. Metal-organic framework nanosheets in polymer composite materials for gas separation. *Nat Mater* **2015**, *14* (1), 48-55. DOI: 10.1038/nmat4113 From NLM PubMed-not-MEDLINE.

(24) Gygi, D.; Bloch, E. D.; Mason, J. A.; Hudson, M. R.; Gonzalez, M. I.; Siegelman, R. L.; Darwish, T. A.;

Queen, W. L.; Brown, C. M.; Long, J. R. Hydrogen Storage in the Expanded Pore Metal–Organic Frameworks M2(dobpdc) (M = Mg, Mn, Fe, Co, Ni, Zn). *Chemistry of Materials* **2016**, *28* (4), 1128-1138. DOI: 10.1021/acs.chemmater.5b04538.

(25) Antek G. Wong-Foy, A. J. M., Omar M. Yaghi. Exceptional H<sub>2</sub> Saturation Uptake in Microporous Metal-Organic Frameworks. *J Am Chem Soc* **2006**, *128*, 3494-3495.

(26) Claudia Zlotea, R. C., Fermin Cuevas, Eric Leroy, Philippe Dibandjo, Christophe Volkinger, Thierry Loiseau, Gérard Fe'rey, Michel Latroche. Pd Nanoparticles Embedded into a Metal-Organic Framework: Synthesis, Structural Characteristics, and Hydrogen Sorption Properties. *J Am Chem Soc* **2010**, *132*, 2991–2997.

(27) *Qiskit: An Open-source Framework for Quantum Computing*; IBM: 2019. <https://zenodo.org/records/2562111> (accessed Mar. 2024).

(28) Zorainy, M. Y.; Gar Alalm, M.; Kaliaguine, S.; Boffito, D. C. Revisiting the MIL-101 metal–organic framework: design, synthesis, modifications, advances, and recent applications. *Journal of Materials Chemistry A* **2021**, *9* (39), 22159-22217. DOI: 10.1039/d1ta06238g.

(29) Ramsahye, N. A.; Trung, T. K.; Scott, L.; Nouar, F.; Devic, T.; Horcajada, P.; Magnier, E.; David, O.; Serre, C.; Trems, P. Impact of the Flexible Character of MIL-88 Iron(III) Dicarboxylates on the Adsorption of n-Alkanes. *Chemistry of Materials* **2013**, *25* (3), 479-488. DOI: 10.1021/cm303830b.

(30) Christian Serre, F. M., Christelle Thouvenot, Marc Nogue's, Gérard Marsolier, Daniel Loue'r, Gérard Fe'rey. Very Large Breathing Effect in the First Nanoporous Chromium(III)-Based Solids: MIL-53 or Cr<sub>III</sub>(OH)·{O<sub>2</sub>C-C<sub>6</sub>H<sub>4</sub>-CO<sub>2</sub>}·{HO<sub>2</sub>C-C<sub>6</sub>H<sub>4</sub>-CO<sub>2</sub>H}<sub>x</sub>·H<sub>2</sub>O<sub>y</sub>. *J Am Chem Soc* **2002**, *124* (45), 13519-13526.

(31) Mohamed Eddaoudi, J. K., Nathaniel Rosi, David Vodak, Joseph Wachter, Michael O'Keeffe, Omar M. Yaghi. Systematic Design of Pore Size and Functionality in Isoreticular MOFs and Their Application in Methane Storage. *Science* **2002**, *295* (18), 469-472.

(32) Li, L.-J.; Qin, C.; Wang, X.-L.; Shao, K.-Z.; Su, Z.-M.; Liu, P.-J. Synthesis and characterization of two self- catenated networks and one case of pcu topology based on the mixed ligands. *CrystEngComm* **2012**, *14* (12). DOI: 10.1039/c2ce06451k.

(33) Robin Lorenz' Anna Pearson, K. M., Dimitri Kartsaklis, Bob Coecke. QNLP in Practice: Running Compositional Models of Meaning on a Quantum Computer. *Journal of Artificial Intelligence Research* **2023**, *76* 1305-1342.

(34) Lambeq 0.4.1., <https://cqcl.github.io/lambeq/index.html>. (accessed Mar. 2024)

(35) Lee, S.; Kim, B.; Cho, H.; Lee, H.; Lee, S. Y.; Cho, E. S.; Kim, J. Computational Screening of Trillions of Metal-Organic Frameworks for High-Performance Methane Storage. *ACS Appl Mater Interfaces* **2021**, *13* (20), 23647-23654. DOI: 10.1021/acsami.1c02471 From NLM PubMed-not-MEDLINE.

(36) Liu, Q.; Cong, H.; Deng, H. Deciphering the Spatial Arrangement of Metals and Correlation to Reactivity in Multivariate Metal-Organic Frameworks. *J Am Chem Soc* **2016**, *138* (42), 13822-13825. DOI: 10.1021/jacs.6b08724 From NLM PubMed-not-MEDLINE.

(37) Phong, J. K.; Cooper, C. B.; Michalek, L.; Lin, Y.; Nishio, Y.; Shi, Y.; Gong, H.; Vigil, J. A.; Ilavsky, J.; Kuzmenko, I.; et al. Sequence-dependent self-assembly of supramolecular nanofibers in periodic dynamic block copolymers. *Journal of Materials Chemistry A* **2024**, *12* (2), 1145-1156. DOI: 10.1039/d3ta06695a.

(38) Rizzuto, F. J.; Dore, M. D.; Rafique, M. G.; Luo, X.; Sleiman, H. F. DNA Sequence and Length Dictate the Assembly of Nucleic Acid Block Copolymers. *J Am Chem Soc* **2022**, *144* (27), 12272-12279. DOI: 10.1021/jacs.2c03506 From NLM Medline.

(39) Stefano Canossa, Z. J., Cornelius Groppe, Zichao Rong, Evelyn Ploetz, Stefan Wuttke, Omar M. Yaghi. System of sequences in multivariate reticular structures. *Nature Reviews Materials* **2023**, *8*. DOI: 10.1038/s41578-022-00482-5.

(40) *Materials Studio 2019*; Accelrys Inc.: 2019. (accessed)

(41) Willems, T. F.; Rycroft, C. H.; Kazi, M.; Meza, J. C.; Haranczyk, M. Algorithms and tools for high-throughput geometry-based analysis of crystalline porous materials. *Microporous and Mesoporous Materials* **2012**, *149* (1), 134-141. DOI: 10.1016/j.micromeso.2011.08.020.

(42) Dubbeldam, D.; Calero, S.; Ellis, D. E.; Snurr, R. Q. RASPA: molecular simulation software for adsorption and diffusion in flexible nanoporous materials. *Molecular Simulation* **2015**, *42* (2), 81-101. DOI: 10.1080/08927022.2015.1010082.

(43) Fischer, M.; Hoffmann, F.; Froba, M. Preferred hydrogen adsorption sites in various MOFs--a comparative computational study. *Chemphyschem* **2009**, *10* (15), 2647-2657. DOI: 10.1002/cphc.200900459 From NLM PubMed-not-MEDLINE.

(44) Dimitri Kartsaklis, I. F., Richie Yeung, Anna Pearson, Robin Lorenz, Alexis Toumi, Giovanni de Felice, Konstantinos Meichanetzidis, S. C., Bob Coecke. lambeq: An Efficient High-Level Python Library for Quantum NLP. *arXiv* **2021**. DOI: arXiv:2110.04236v1

(45) Rajashekharaih, K. M. M.; Chickerur, S.; Hegde, G.; Bhat, S. L.; Sali, S. A. Sentence Classification Using Quantum Natural Language Processing and Comparison of Optimization Methods. In *Advanced Computing*,

Communications in Computer and Information Science, 2023; pp 85-98.

(46) Spall, J. C. Implementation of the Simultaneous Perturbation Algorithm for Stochastic Optimization. *IEEE Transactions on Aerospace and Electronic Systems* **1998**, *34* (3), 817-823.

(47) Bird, S., Edward Loper, Ewan Klein. Natural Language Processing with Python. *O'Reilly Media Inc.* **2009**.

Supplementary information for:

# Inverse Design of Metal-Organic Frameworks Using Quantum Natural Language Processing

*Shinyoung Kang, Jihan Kim\**

Department of Chemical and Biomolecular Engineering, Korea Advanced Institute of  
Science and Technology (KAIST) 291 Daehak-ro, Yuseong-gu, Daejeon 34141, Republic of  
Korea

## Table of Contents

**Supplementary Figure S1.** Building blocks of MOF dataset

**Supplementary Figure S2.** Scatter plot showing a correlation between pore volume and MOF gravimetric H<sub>2</sub> uptake

**Supplementary Note S1.** MOF representation based on QNLP models

**Supplementary Figure S3.** String diagrams of MOF representation based on QNLP models and their corresponding quantum circuits.

**Supplementary Figure S4.** String diagram of MOF ‘pcu N248 E70’ based on DisCoCat model after applying reduction rules.

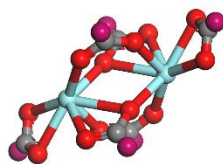
**Supplementary Figure S5.** Training history of multi-class classification based on BoW model

**Supplementary Table S1.** A detailed test results of generating MOF with target property

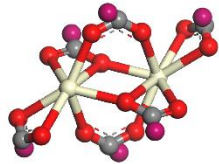
**Supplementary Figure S6.** MOF structures that have low, moderately low, moderately high, and high pore volume and H<sub>2</sub> uptake values

**Supplementary Table S2.** Results of hyperparameter test

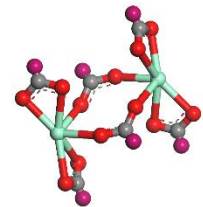
(a)



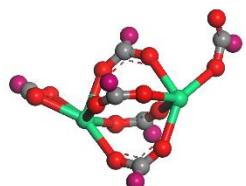
N106  
Source: LALPIZ\_clean  
Formula: Y<sub>2</sub>C<sub>6</sub>O<sub>12</sub>X<sub>6</sub>



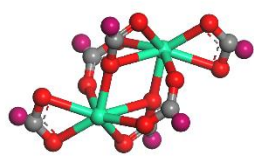
N123  
Source: ALUKIC\_clean  
Formula: Ce<sub>2</sub>C<sub>6</sub>O<sub>12</sub>X<sub>6</sub>



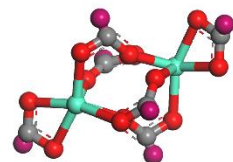
N139  
Source: KULRIT\_clean  
Formula: Yb<sub>2</sub>C<sub>6</sub>O<sub>12</sub>X<sub>6</sub>



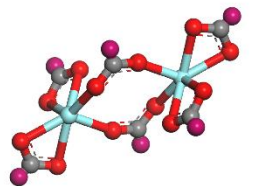
N144  
Source: GAJVAQ\_clean  
Formula: Er<sub>2</sub>C<sub>6</sub>O<sub>12</sub>X<sub>6</sub>



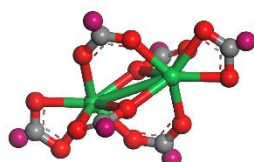
N155  
Source: BETDAH\_clean  
Formula: Ho<sub>2</sub>C<sub>6</sub>O<sub>12</sub>X<sub>6</sub>



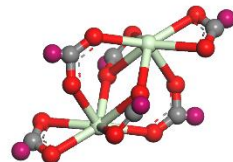
N173  
Source: ETEKAQ01\_clean5b  
Formula: Gd<sub>2</sub>C<sub>6</sub>O<sub>12</sub>X<sub>6</sub>



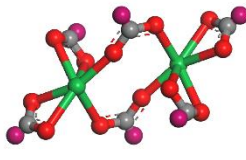
N205  
Source: LAGMUD\_clean  
Formula: Y<sub>2</sub>C<sub>6</sub>O<sub>12</sub>X<sub>6</sub>



N248  
Source: KULRIT\_clean  
Formula: Yb<sub>2</sub>C<sub>6</sub>O<sub>12</sub>X<sub>6</sub>



N394  
Source: BETFEN\_clean  
Formula: Pr<sub>2</sub>C<sub>6</sub>O<sub>12</sub>X<sub>6</sub>



N505  
Source: LAGRIW\_clean  
Formula: Yb<sub>2</sub>C<sub>6</sub>O<sub>12</sub>X<sub>6</sub>

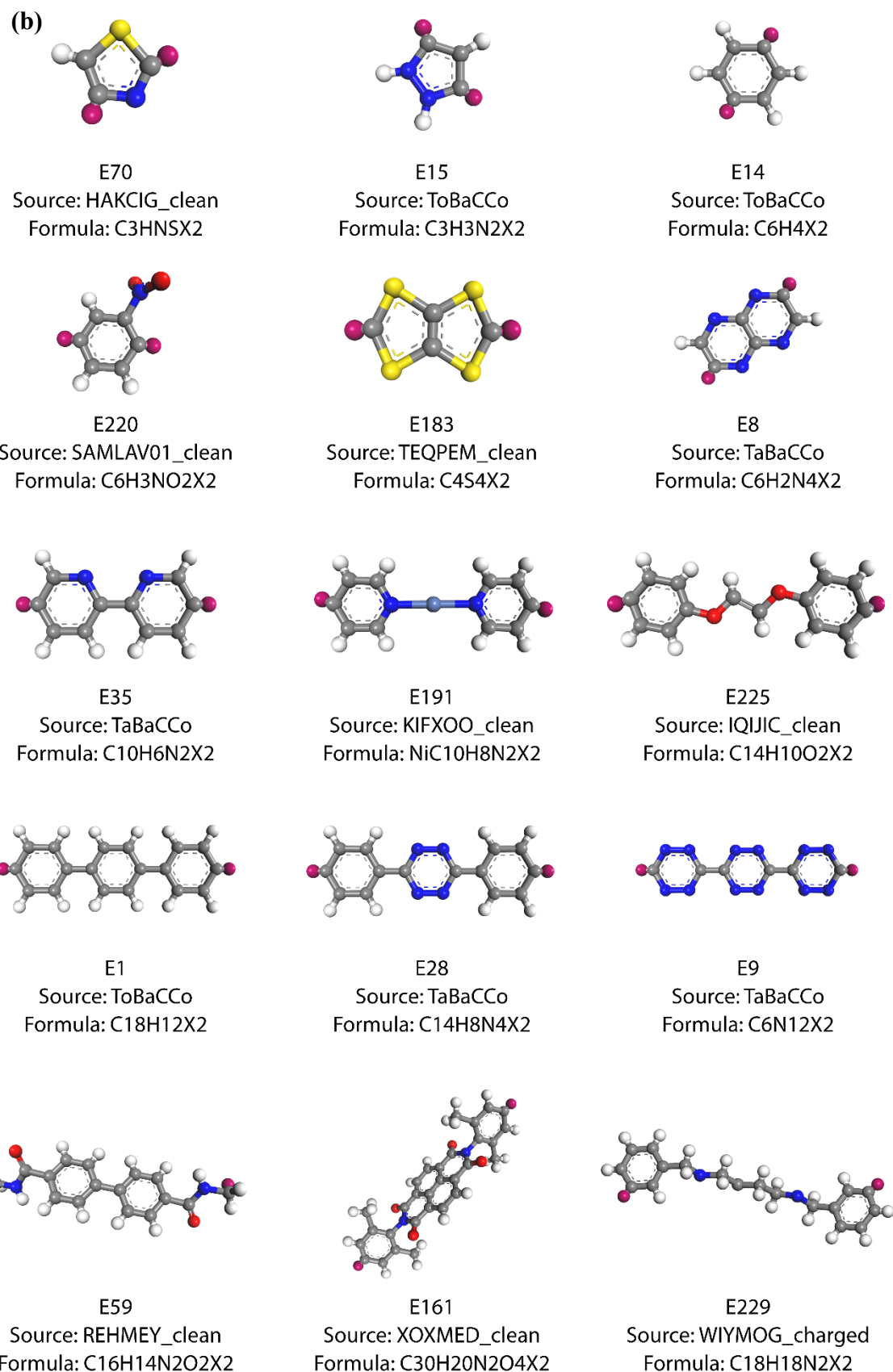


**Figure S1.** Building blocks of MOF dataset: **(a)** node and **(b)** edge. X indicates the connection point with building blocks.

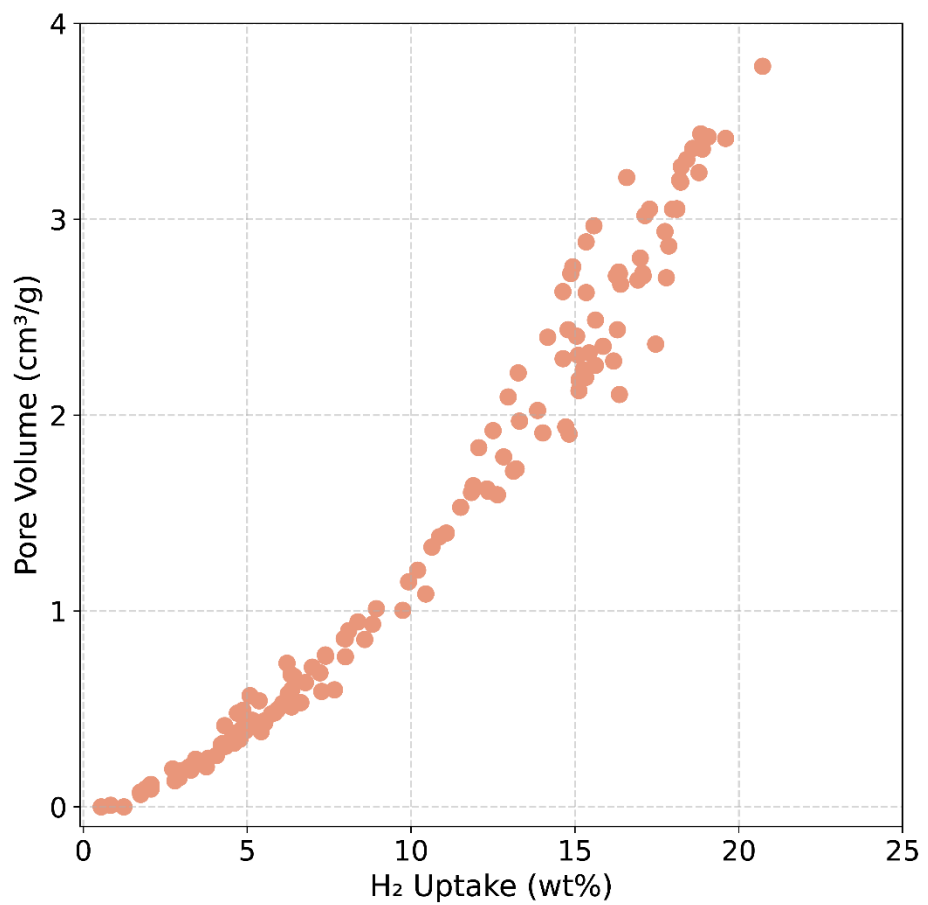


**Figure S2.** Scatter plot showing a correlation between pore volume and MOF gravimetric H<sub>2</sub> uptake.

### Note S1: MOF Representation based on QNLP Models

Given that our MOF dataset is organized by its modular components (i.e. topology, node, and edge) similarly to how sentences are formed from a selection of words, it is well-suited for the direct application of various QNLP models to construct string diagrams, the quantum version of tensor networks. The DisCoCat model processes the data based on Combinatory Categorial Grammar (CCG)<sup>1</sup>, which is designed for linguistic parsing, and it focuses on the syntactic and semantic relationships between words in a sentence. In this context, a MOF can be viewed as a noun phrase atomic type,  $n$ , where the edge acts as a relative pronoun atomic type,  $n$ , and the node and the topology function as a left adjoint (i.e.,  $n.l$ ) and a right adjoint (i.e.,  $n.r$ ), respectively (Figure 3a). The pregroup grammar in DisCoCat has two reduction rules<sup>2</sup>:

$$p \cdot p^r \rightarrow 1 \quad p^l \cdot p \rightarrow 1 \quad (1)$$

where  $p$  denotes atomic type. Thus, the pregroup string diagram for MOF such as “pcu N248 E70” is represented by  $(n \cdot (n^l \cdot n) \cdot n^r) \cdot n$  and the derivation for single MOF is reduced to  $(n \cdot (n^l \cdot n) \cdot n^r) \cdot n \rightarrow n \cdot 1 \cdot n^r \cdot n \rightarrow (n \cdot n^r) \cdot n \rightarrow 1 \cdot n \rightarrow n$  based on aforementioned reduction rules. Although its pregroup grammar was not designed for chemical structures like MOFs, we decided to include this fully-syntax sensitive model for comparative purposes. The transition from these pregroups to vector space semantics is processed by mapping each type to a vector space ( $n$  to a vector space  $N$ ) and composite types to corresponding tensor product spaces ( $n^r \cdot n$  to a tensor product space  $N \otimes N$ )<sup>3</sup>. As shown in Figure S3a, boxes in the DisCoCat string diagram represent tensors, the order of which is determined by the number of their wires, and the cups (U-shape wire denoting  $n^l \cdot n$  or  $n \cdot n^r$ ) are the tensor contraction governed by the reduction rules. After applying reduction rules, the string diagram is further simplified as shown in Figure S4. The transformation to the quantum circuit is achieved by the selection of ansatz and each MOF component vector being mapped into individual qubits (Figure S3d). The specific arrangement of unitary operations in the circuit will not be discussed since this is beyond the scope of this paper, but it is basically based on the compositional and reduction rules from the DisCoCat model.

Lastly, two types of word-sequence approaches were considered, and these models are the quantum version of a simple recurrent neural network (RNN). The word-sequence model captures the order of the MOF components. A tensor,  $s$ , represents each MOF component with the multiplication of the corresponding adjoint type,  $s.r$ , and the sequential multiplication of these tensors in the order becomes the MOF as the output vector. This process begins with the “start” token vector and the connectivity of each component with left-to-right

sequence is represented as cups as demonstrated in Figure S3b. Here, all component vectors, including the “start” vector, are mapped into the individual qubits, and the unitary operations reflect the MOF structure as defined by the sequential multiplication of its components (Figure S3e). Another word-sequence approach available in lambeq<sup>2</sup> involves the use of a “stair” instance, which executes the tensor multiplication sequentially from left to right (Figure S3c). In this case, the stair instance is encoded as a unitary operation within the quantum circuit. So this approach can be an economical option since it generates the output without the additional “start” token and the adjoint vectors (Figure S3f).

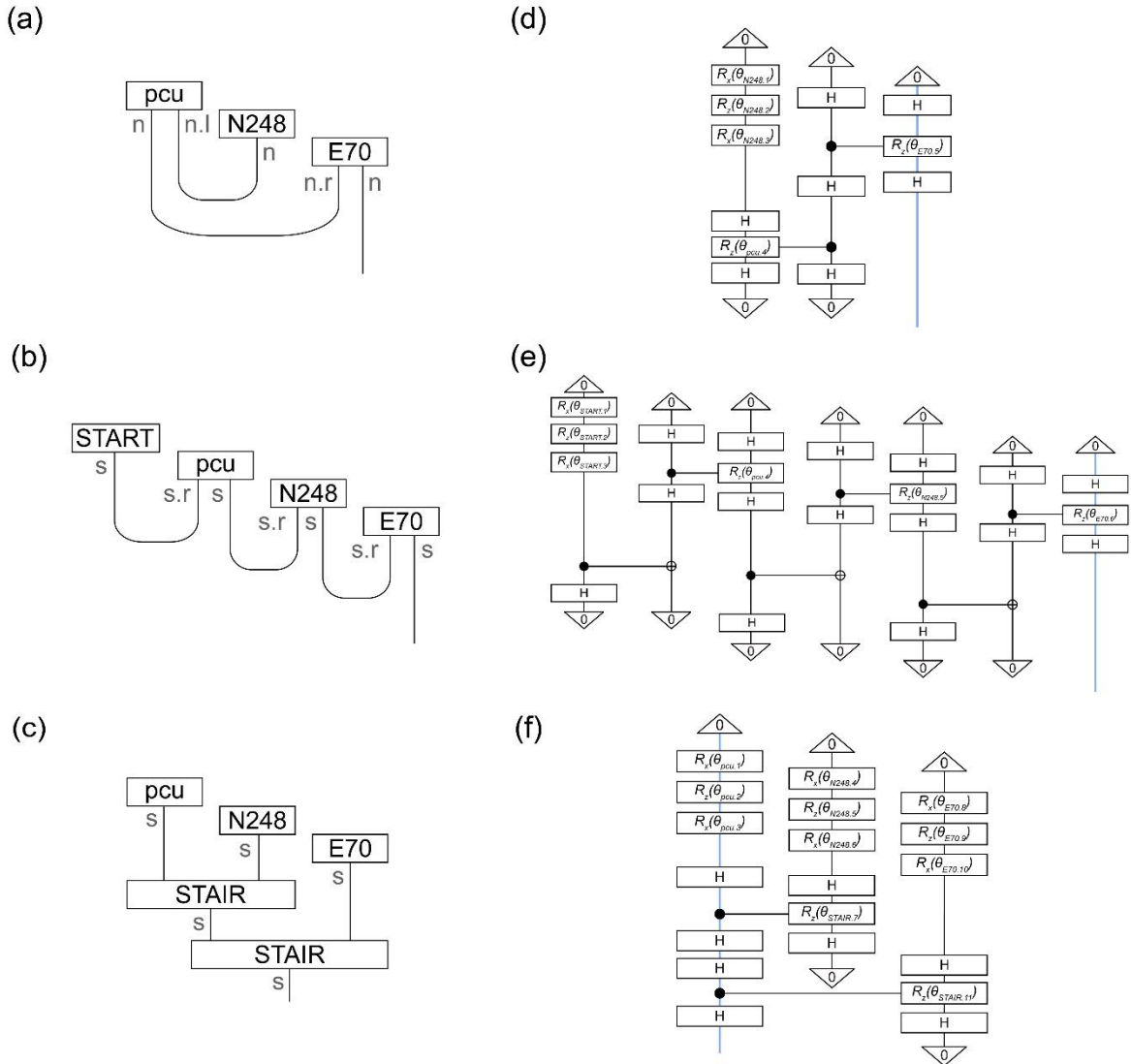


**Figure S3.** String diagrams of MOF representation based on (a) DisCoCat model, (b) word-sequence model, and (c) word-sequence model with a stairs-like recurrent manner. Their corresponding quantum circuits based on IQP ansatz were shown in (d), (e), and (f) for DisCoCat, word-sequence, and stair models, respectively. Open-wire that carries predicted class label is highlighted as blue line.

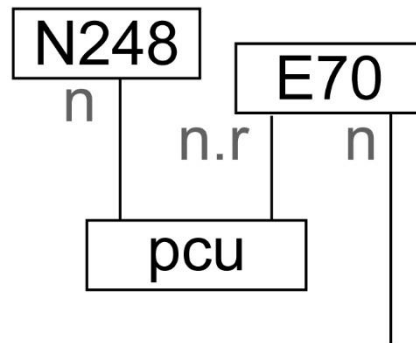


**Figure S4.** String diagram of MOF ‘pcu N248 E70’ based on DisCoCat model after applying reduction rules.

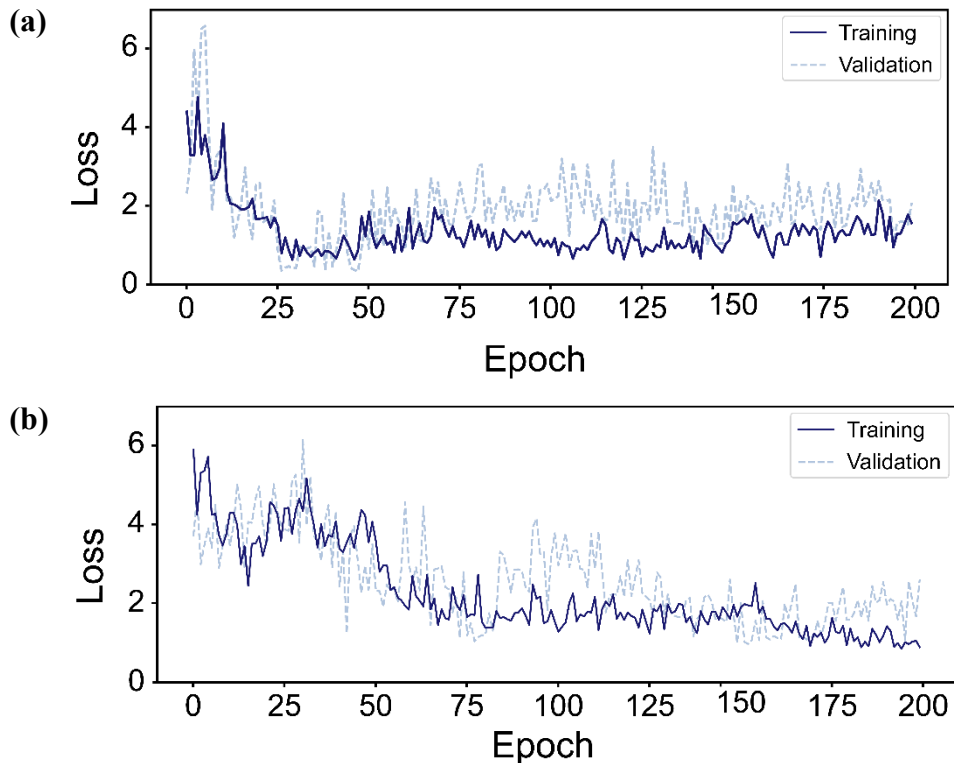


**Figure S5.** Training history of multi-class classification based on BoW model for **(a)** pore volume and **(b)** H<sub>2</sub> uptake dataset.

**Table S1.** A detailed test results of generating MOF with target property.

Target Property		Correct	Incorrect	Timeout	Avg. guess
Pore volume	Low	100	0	0	9.03
	Mod. Low	96	1	3	26.56
	Mod. High	86	14	0	15.09
	High	92	7	1	22.79
H <sub>2</sub> uptake	Low	93	4	3	20.33
	Mod. Low	91	8	1	17.68
	Mod. High	90	0	10	37.8
	High	82	13	5	30.75

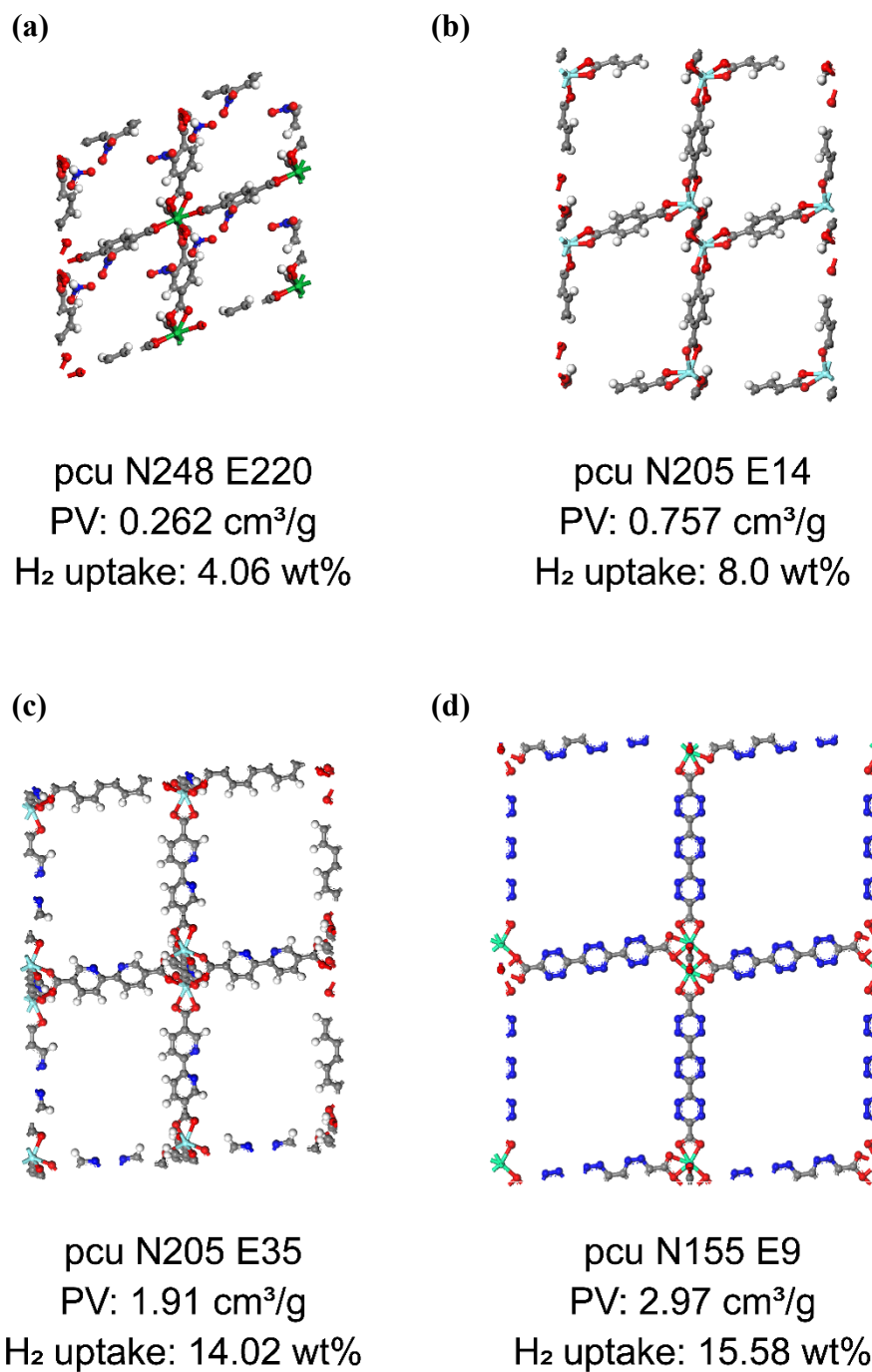


**Figure S6.** MOF structures that have **(a)** low, **(b)** moderately low, **(c)** moderately high, and **(d)** high pore volume and H<sub>2</sub> uptake values.

**Table S2.** Results of varying the stability constant, A, based on pore volume and H<sub>2</sub> uptake datasets. The selected parameter setup for the model was highlighted in gray color.

A	metric	Model 00		Model 01		Model 10		Model 11		
		train	validation	train	validation	train	validation	train	validation	
Pore volume	0.1	loss	0.223	0.216	0.363	0.517	0.326	0.557	0.239	0.251
		accuracy	0.893	0.879	0.812	0.879	0.847	0.818	0.911	0.879
	0.01	loss	0.216	0.278	0.375	0.499	0.303	0.493	0.182	0.217
		accuracy	0.893	0.818	0.859	0.818	0.888	0.818	0.94	0.909
	0.001	loss	0.227	0.432	0.397	1.04	0.238	0.722	0.173	0.421
		accuracy	0.905	0.879	0.788	0.788	0.924	0.788	0.94	0.879
H <sub>2</sub> uptake	0.1	loss	0.164	0.897	0.395	0.622	0.417	0.478	0.212	0.98
		accuracy	0.94	0.848	0.776	0.788	0.847	0.788	0.929	0.848
	0.01	loss	0.265	0.466	0.293	0.639	0.439	0.439	0.221	0.966
		accuracy	0.845	0.848	0.906	0.727	0.806	0.788	0.917	0.818
	0.001	loss	0.207	0.371	0.33	0.658	0.439	0.492	0.201	0.483
		accuracy	0.917	0.818	0.871	0.788	0.788	0.758	0.881	0.848

## References

- (1) Clark, S. Something Old, Something New: Grammar-based CCG Parsing with Transformer Models. *arXiv* **2021**. DOI: arXiv:2109.10044v2.
- (2) Dimitri Kartsaklis, I. F., Richie Yeung, Anna Pearson, Robin Lorenz, Alexis Toumi, Giovanni de Felice,; Konstantinos Meichanetzidis, S. C., Bob Coecke. lambeq: An Efficient High-Level Python Library for Quantum NLP. *arXiv* **2021**. DOI: arXiv:2110.04236v1
- (3) Robin Lorenz' Anna Pearson, K. M., Dimitri Kartsaklis, Bob Coecke. QNLP in Practice: Running Compositional Models of Meaning on a Quantum Computer. *Journal of Artificial Intelligence Research* **2023**, 76 1305-1342.